

Force transmission and dissipation in dynamic compression of architected metamaterials

T. GÄRTNER ^{ab*}, S.J. VAN DEN BOOM ^{bc}, J. WEERHEIJM^a, AND L.J. SLUYS ^a

^aFaculty of Civil Engineering and Geosciences, Delft University of Technology

^bNetherlands Institute for Applied Scientific Research (TNO)

^cFaculty of Mechanical Engineering, Delft University of Technology

* *Corresponding author: t.gartner@tudelft.nl*

29th August 2025

Abstract

Materials engineered with an internal architecture in order to achieve unusual properties, so-called mechanical metamaterials, are a promising candidate in the ongoing quest for lightweight impact mitigation. During impact events, these materials are subject to high strain rates, and the forces occurring due to the deceleration of the impactor are transmitted in a non-uniform way. The prevailing research in the field of impact mitigation focuses largely on the global effects of architected materials, with less attention being paid to the internal mechanisms of these structured materials. While there have been recent studies on the distribution of forces throughout an impact event, less research is devoted to the transmission of forces and the distribution of energy dissipation. The objective of this study is to examine the transition from static deformation patterns to dynamic phenomena for different types and sizes of microstructure, and to understand both the force transmission through the patch and the energetic distributions in different strain rate regimes. To enable this investigation discretized—geometrically as well as materially—nonlinear Timoshenko-Ehrenfest beams are used in implicit and explicit finite element schemes. The transmitted force levels and energy dissipation are investigated for two auxetic architectures (one for each mechanism resulting in a negative Poisson’s ratio) and one non-auxetic architecture. The dynamic force levels transmitted to the back face exhibit an initial peak of a similar magnitude for all investigated strain rates and stabilize to the static stress plateau for each architecture. While the global amount of potential energy remains largely unchanged for all investigated rates, the amount of dissipation and kinetic energy demonstrates a non-linear increase from static deformation to slow and high rate deformation. The phenomena observed in different architectures are highlighted, and the differences are explained and related back to the configurations of the lattices. Notably, the prevalent notion in literature asserting the superiority of negative Poisson’s ratio materials for impact mitigation applications is not replicated in this study.

Keywords

Architected materials; Impact mitigation; Strain-rate effects; Elasto-plastic beams; Dynamic compression

1 Introduction

The engineered microstructure of architected materials achieving unusual mechanical properties, resulting in so-called mechanical metamaterials, presents new opportunities for designers and engineers and new challenges for researchers [22, 3, 41]. Of particular interest is the design of metamaterials for impact mitigation. Impact events, necessitating protective measures, exist in a wide range of fields, from sports [35] over space travel [29], metal roofs in hailstorms [34], collisions between cars and civil infrastructure [28] to personal protective equipment [11]. In all these applications, the aim of the protective structure is to limit the energy and impulse transmitted from the impactor to the protected structure, be it a living being or an otherwise fragile material.

In this quest, auxetic (negative Poisson’s ratio) materials have gained considerable interest in the research community in recent years, as evidenced by the reviews [2, 42, 32, 36]. The negative Poisson’s ratio, which characterizes auxetic materials, leads to lateral material contraction under compression, as shown in Figure 1.1. For impact mitigation, auxetic materials are of special interest due to reported higher indentation resistance [1] as well as shear resistance [6]. Other promising properties for impact mitigation include increased fracture toughness [5] and enhanced energy absorption [21]. Auxetic materials naturally compress themselves underneath the impacted area, reportedly allowing for more mass-efficient protective solutions. However, these assumptions are based on homogeneous, isotropic materials under infinitesimal, quasi-static deformation.

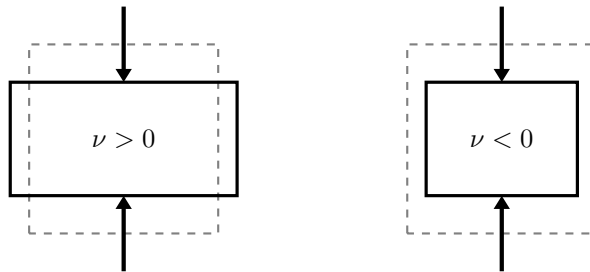


Figure 1.1: Auxetic materials concept.

As no relevant natural auxetic materials exist, this negative Poisson effect needs to be artificially created through mechanical metamaterials. Whilst mechanical metamaterials can be constructed from shells [25], plates [18, 24], or as foams [10], the focus in this work is on auxetic structures based on structured beam-lattices. These architected materials are inherently *not* isotropic and, as they also undergo large deformations, their material properties vary throughout deformation. In beam lattices, the individual beams are re-oriented, leading to a change in the effective material properties [14].

As shown in [15] not only the pure energy absorption capability of a structure is of importance for impact mitigation, but also the—temporal and spatial—distribution of forces. In the present contribution, further investigation is conducted into the distribution of energy dissipation within the structure at varying strain rates for different refinement levels, alongside the subsequent effects on the force transmission from the impactor to the protected structure.

The investigation into the energy absorption of protective structures has thus far focused mostly on the energy dissipated by compression of the structure, and its conclusions focus on the higher amount of energy dissipated by auxetic lattices [30, 23]. However, little attention is given to the internal mechanisms and the distribution of the energies in comparable metamaterials of different architectures. Investigations of different collapse patterns under high speed compression were undertaken as early as the 1980s [4], where a comparison between two types of structures and their internal collapse mechanism is shown. Ruan et al. [33] investigated different modes of collapse occurring throughout different speeds in non-auxetic conventional honeycombs with different wall-thicknesses. More recently, investigations into the static mechanisms in the deformation of metamaterials, either driven by the boundary conditions [7] or by the interaction between local and global collapse patterns [44] have been conducted. However, only one type of fundamental architecture was investigated in all these works, and a comparison between different auxetic and non-auxetic architectures is yet to be made. The link between the collapse patterns, dynamic loading and the corresponding force transmission for different types of unit cells is explored in this manuscript. To provide a first insight into this topic, numerical experiments are conducted

using beam-based finite element analyses. For these analyses, three different fundamental unit cells, are investigated: **a)** the most common auxetic type, a re-entrant honeycomb (cf. [17]); **b)** an auxetic cell based on a rotation mechanism, the so-called missing ribs or chiral unit cell (cf. [39]); and **c)** a non-auxetic unit cell, the regular honeycomb. The three unit cells are designed to exhibit the same relative density as well as initial stiffness (cf. [14]). Knowledge of the behaviour of these architectures will allow for better insight into the mechanisms of collapse under different strain rates. Here, special attention will be paid to the effects of microstructural refinement and transmission of forces from the strike face of the protective layer, i.e. the side of the structure subjected to the impact, to its back face, i.e. the interface with the opposing structure. This enables design engineers to decide on a protection concept fit for the expected impact events.

The architecture designs for the investigated metamaterials are presented in Section 2, and in Section 3 the numerical framework to conduct the investigation is laid out. In Section 4, an investigation into the static behaviour of different sizes of unit cells in a patch is presented, which forms the basis for the investigation into the force transmission at different rates through the patch in Section 5. To understand the processes involved in this force transmission better and obtain insight into the deformation patterns, in Section 6, the distribution of energies is presented and discussed. The article closes in Section 7 with a short discussion of the obtained results, limitations of this study and recommendations for further research.

2 Investigated architectures

All architectures investigated are designed to exhibit a Young's modulus of 300 MPa in vertical direction and a relative density with regard to the base material of 0.1. The material of which the architectures are constructed from is taken to be a steel with a Young's modulus of 210 GPa, a Poisson's ratio of 0.3, and a density of 7850 kg m^{-3} . An in-depth discussion on the static, elastic properties of these architectures, as well as the design process, can be found in [14]. It should, however, be noted that the absolute dimensions of the unit cells do not matter for the determination of the Young's modulus or the relative density, so that the unit cell can be directly scaled to the desired measures for the investigations conducted in this work.

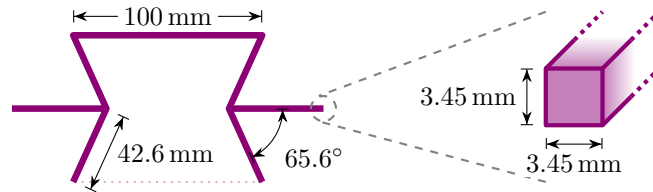


Figure 2.1: Re-entrant unit cell used throughout this investigation.

The first investigated unit cell is the most common auxetic architecture, the re-entrant honeycomb (cf. [17]). Its configuration is shown in Figure 2.1. The horizontal beam has a length of 100 mm, the tilted beams a length of 42.6 mm and the angle between the titled beams and the horizontal is set to be 65.6° . The beams itself have a square cross-section with a side length of 3.45 mm.

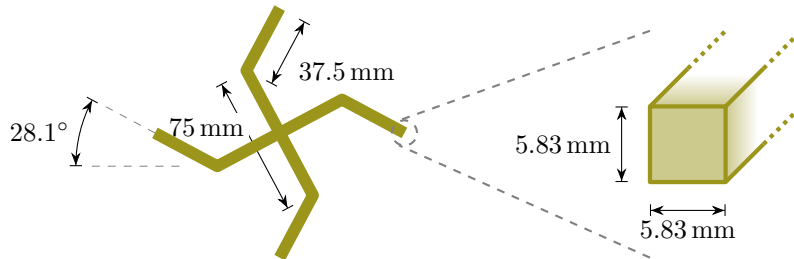


Figure 2.2: Chiral unit cell used throughout this investigation.

In order to also capture unit cells with a fundamentally different deformation mechanism, chiral,

sometimes called missing ribs, unit cells (cf. [39]) are investigated. Whilst the Poisson effect of re-entrant honeycombs is driven largely by inwards folding, the deformation of chiral unit cells is driven by rotation of the joints, resulting in a mechanism that can also be found in rotating squares unit cells (e.g. [7]). The chiral unit cell is depicted in Figure 2.2. The length of a single beam in the centre is 75 mm and the angle between the horizontal (or vertical) axis and the beams is set to 28.1° . This results in a width of the entire unit cell of 132 mm and together with a square cross-section of 5.83 mm side length, the relative density of 0.1 and the effective Young's modulus of 300 MPa in vertical direction are obtained as for the re-entrant unit cell.

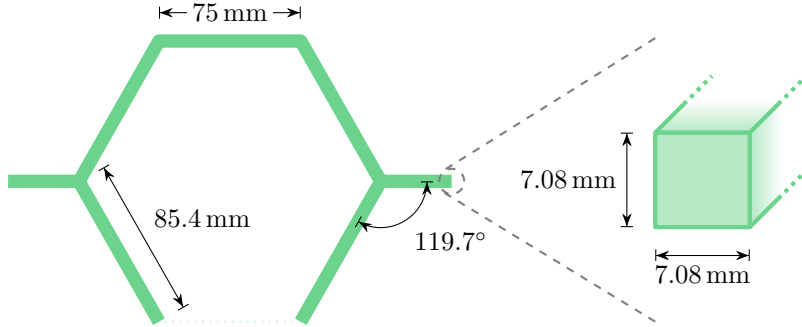


Figure 2.3: Honeycomb unit cell used throughout this investigation.

The final investigated unit cell is the non-auxetic honeycomb as depicted in Figure 2.3. The horizontal beam has a length of 75 mm and the tilted beams are 85.4 mm long. The beams have a square cross-section with a side length of 7.08 mm and the angle between the tilted beams and the horizontal is set to 119.7° . Again, the resulting Young's modulus and relative density are 300 MPa in vertical direction and 0.1, respectively.

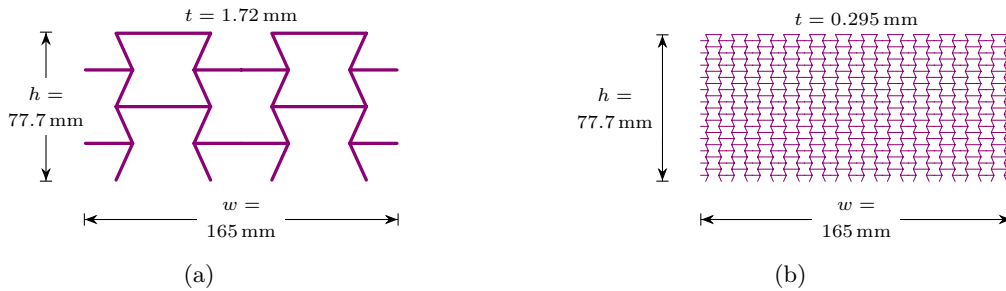


Figure 2.4: Patches from 2×2 and 12×12 unit cells, scaled to ensure the same outer dimensions.

All three unit cells are subsequently assembled into patches. When assembling these patches, the unit cells are scaled down, to ensure that the overall patch has the same outer dimensions for each architecture. For the scaling, all geometric dimensions, the length of the beams, as well as the dimensions of their cross-sections are scaled by the same factor. The thickness in the third direction is thus changing for a different number of unit cells, which is accounted for in the later analyses. A comparison between two patches consisting of 2×2 and 12×12 unit cells is shown in Figure 2.4. In this illustration, the scaling of the singular unit cells to achieve the same outer dimension is shown.

3 Numerical framework

The implementation for this work uses the JIVE-Framework [13].

In order to model patches made from the unit cells described above, the lattices are subsequently modelled as a collection of nonlinear Timoshenko-Ehrenfest beams. These beams are also called special Cosserat rods, geometrically exact beams or Simo-Reissner beams after [31, 37]. Such beams can be described by the position of their centreline and the orientation of the cross-sections along the centreline.

The resulting six-dimensional space of strain-prescriptors corresponds with a six-dimensional space of stress-resultants. For the initial, elastic response of the beams, a Young's modulus of $E = 210$ MPa and a Poisson's ratio of $\nu = 0.3$ are assumed.

For plastic material behaviour of the beam, a direct approach is used incorporating plasticity into the beam-level variables as discussed in [16]. The yield function Φ and hardening tensor \mathbf{H} for a reference quadratic cross-section of side length 0.75 mm are taken to be

$$\Phi = \left| \frac{N_1}{71.8 \text{ N} - N_1^h} \right|^{2.68} + \left| \frac{N_3}{164 \text{ N} - N_3^h} \right|^{1.75} + \left| \frac{M_2}{30.8 \text{ N mm} - M_2^h} \right|^{1.93} - 1, \quad (1)$$

$$\mathbf{H} = \begin{bmatrix} 936 \text{ N} & 1630 \text{ N} & 618 \text{ N mm} \\ & 2800 \text{ N} & 907 \text{ N mm} \\ \text{sym.} & & 443 \text{ N mm}^2 \end{bmatrix}. \quad (2)$$

The stress resultant N_1 represents the shear force, N_3 the axial force, and M_2 the bending moment. The hardening tensor determines the kinematic hardening present in the beam-plasticity formulation and subsequently the evolution of the yield surface represented by the hardening contributions N_1^h , N_3^h , M_2^h . For a deeper treatise, the reader is referred to [40, 20, 16]. These parameters resulted from scaling the reported values from literature [19, 20] to the physical material parameters of the steel used in earlier experiments [15]. Scaling of these parameters follows the approaches given in [19, 16].

The approach of Simo and Vu-Quoc [38] and subsequent improvements proposed by Crisfield and Jelenić [9] are followed to determine the global stiffness matrix and resulting nodal forces. Throughout the analysis, beams are discretized using linear elements with Lagrangian shape functions and uniformly reduced integration to avoid shear-locking phenomena.

Contact between the beams is implemented following [43]. We assume frictionless contact between two linear two-node elements. For each node-to-element pairing the contact forces are computed using a penalty approach. In order to scale the contact stiffness with the size of the contact points, the penalty parameter ε is adapted with the thickness of the beams t

$$\varepsilon = 1 \times 10^7 \cdot \left(\frac{t}{1 \text{ mm}} \right)^2, \quad (3)$$

as the contact radii around all beams are set to half the beam thickness

$$r = \frac{t}{2}. \quad (4)$$

For the static investigations an implicit Newton-Raphson scheme is employed, whilst the dynamic investigations are computed using an explicit scheme with adaptive time stepping. This adaptive stepping scheme uses an explicit and implicit Euler scheme as a predictor-corrector pair and a Milne-device [26] as error estimator. The orientation matrices, being of the special orthogonal group $\text{SO}(3)$, are integrated using an exponential integrator (e.g. [27]).

Throughout the analysis, different stress and energy measures are recorded. The stress on the strike face is the sum of the resulting nodal forces in vertical direction on the top boundary divided by the width of the sample w and the thickness t of a beam. A similar computation is employed for the back face. As the resulting forces on the strike face are typically acting downwards (in negative direction) a factor of -1 is added to obtain positive values:

$$\sigma_{\text{strike}} = -1 \cdot \frac{\sum f_{\text{strike}}}{wt}, \quad (5)$$

$$\sigma_{\text{back}} = \frac{\sum f_{\text{back}}}{wt}. \quad (6)$$

The specific energy absorption (SEA), i.e. the external work put into the system, is calculated by integrating the sum of the resulting forces on the strike face over the displacement of the strike face u_{strike} and normalizing it by the mass of the patch m_{patch} :

$$\text{SEA}(u) = \frac{1}{m_{\text{patch}}} \int_0^u \left(\sum f_{\text{strike}} \right) du_{\text{strike}}, \quad (7)$$

where the integration is executed using the discrete values recorded during the simulation using Simpson's rule. The potential, kinetic and dissipated energies are recorded on a nodal basis. The kinetic energy is directly computed from the nodal velocities and the global mass matrix, whereas the potential and dissipated energies are calculated per element and subsequently integrated for each node using standard finite element procedures.

As the time-steps for the different simulations are not identical, and the dynamic simulations conducted show high-frequency oscillations due to the absence of damping in the model, all reported measures are created from the average of bins stretching 0.5% compression each. E.g. the point plotted at 15% compression is the average of the recorded values between 14.75% and 15.25% compression.

3.1 Boundary conditions

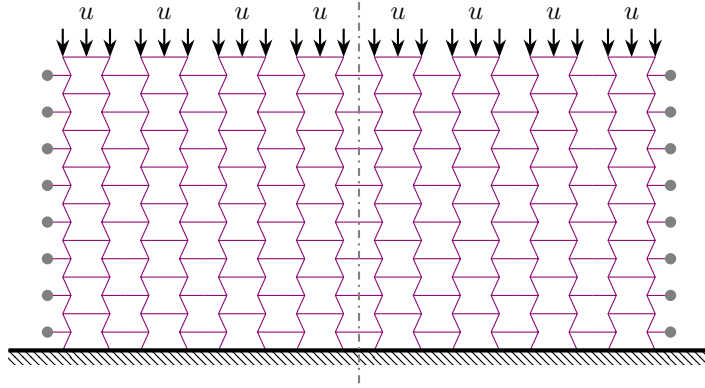


Figure 3.1: Boundary conditions applied in this investigation at the example of an 8×8 patch.

In order to estimate the behaviour of different patch configurations, a set of boundary conditions mimicking a constant strain-rate setup is applied. An overview of these boundary conditions can be found in Figure 3.1. On the bottom side, the patch is fully fixed, whilst at the top side, horizontal movement is prevented and a vertical, compressive displacement $u = u_{\text{strike}}$ is enforced. The boundary nodes on the left and on the right side are enforced to deform symmetrically with respect to a symmetry plane corresponding to the centre of the patch, in order to prevent globally asymmetric deformation.

Throughout this study, different compression rates \dot{u}/h are investigated. As a reference case *static* compression is analysed. For the dynamic investigations, the investigated strain rates are $\dot{u}/h = 250 \text{ s}^{-1}$, $\dot{u}/h = 1000 \text{ s}^{-1}$, and $\dot{u}/h = 4000 \text{ s}^{-1}$. These rates will be called in the remainder of the manuscript *slow* rate compression ($\dot{u}/h = 250 \text{ s}^{-1}$), *medium* rate compression ($\dot{u}/h = 1000 \text{ s}^{-1}$), and *fast* rate compression ($\dot{u}/h = 4000 \text{ s}^{-1}$).

4 Effects of the number of unit cells

As a first investigation, using the boundary conditions described above, the effect of the number of unit cells within the patch is analysed. For this, unit cells of different size are assembled into patches of the same overall size, ensuring the same elastic tangent properties, as explained in Section 2 and shown in Figure 2.4. This scaling results in e.g. each individual unit cell in a 2×2 patch to be twice as high and wide as each individual unit cell in a 4×4 patch. The resulting changes in the thickness of the patch in the third dimension t are explicitly accounted for when calculating the stresses in Equations (5) and (6) and implicitly via the total mass m_{patch} when calculating the SEA in Equation (7).

4.1 Re-entrant unit cells

The behaviour of different re-entrant patches under *static* compression is investigated first. In Figure 4.1 the *static* stress-strain curves at the strike face for different numbers of re-entrant unit cells under compression are shown. All investigated patches show onset of plasticity at 1% compression. Prior

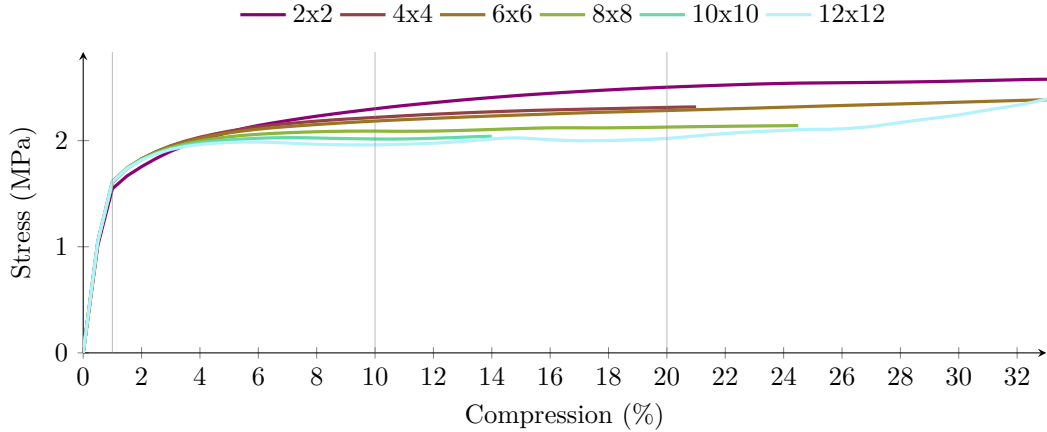


Figure 4.1: Stress-strain curves of patches with a different number of re-entrant unit cells under *static* compression.

to the onset of plasticity, there is some loss of stiffness corresponding with the re-orientation of beams and the subsequent shift in load-carrying capacity as discussed in [14]. After the onset of plasticity, as the load carrying capacity of the beams is limited at yield, nearly no stiffness remains upon further deformation. When the unit cell size is decreased, a more brittle response is observed. This phenomenon is attributed to the more pronounced localization resulting from the smaller unit cells, and thus in less material undergoing large deformations. The hardening in later stages of the response, most clearly seen for the 12×12 patch, is an effect of contact within the unit cells.

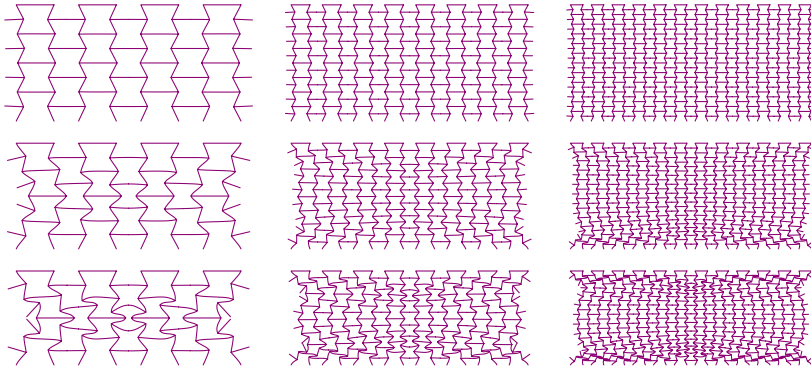


Figure 4.2: Re-entrant 4×4 (left), 8×8 (centre), and 12×12 (right) unit cell patches under *static* deformation at 1%, 10% and 20% compression.

The deformation patterns in Figure 4.2 support this observation. In this figure, the deformed configurations of 4×4 , 8×8 , and 12×12 unit cell patches are showcased for 1%, 10% and 20% compression. These compression levels are indicated by vertical lines in Figure 4.1 as well. Here, it can be seen, that 1% compression coincides with the loss of stiffness due to plasticity. During the initial, mostly elastic deformation (depicted in the top row), the patches are deformed uniformly. At a deformation of 10%, differences in deformation are visible: Whereas in the 4×4 and the 8×8 patch, on the left and in the centre, the deformation appears symmetric both along the vertical axis as well the horizontal axis, the 12×12 patch on the right side of the figure shows a break of symmetry along the horizontal axis, i.e. the deformation of the top half does not mirror the deformation of the bottom half. This is due to a localization of deformation near the bottom edge. A stronger deformation within a single row of unit cells leads to a stronger loss in stiffness and a more brittle response. Once such a weak spot appears, the remaining deformation concentrates around it. In the last row of Figure 4.2, the deformation state for 20% compression is shown. Here, the localization is intensified and becomes visible for the 8×8 unit cell patch in the centre of the figure as well, whilst the 4×4 patch on the left maintains both symmetries. All

investigated patches suffer from loss of convergence in the global Newton-Raphson scheme at different stages of compression. The common cause of these numerical problems is the contact between free ends of beams at the left and right boundaries of the patch, as can be seen for example in the centre of the 4×4 unit cell patch at both sides between the second and third unit cell.

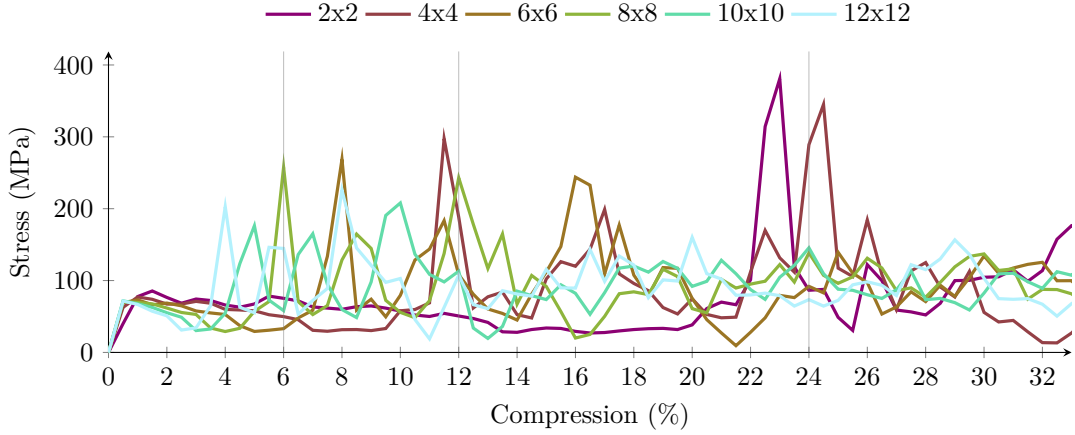


Figure 4.3: Stress-strain curves of patches with a different number of re-entrant unit cells under *fast* rate compression.

For the investigations of the impact behaviour of architected metamaterials, the consideration of dynamic deformation is of crucial importance. To this end, the effects of different numbers of unit cells on the dynamic response of a patch are investigated as well. In Figure 4.3 the stress-strain curves measured at the strike face for *fast* rate compression are shown. For all patches, an initial rise in the stress can be observed, followed by a loss in stiffness, that is occurring earlier for smaller unit cells. Prior to the onset of plasticity at around 1%, smaller unit cells show a more stiff response, attributed to differences in the distribution of inertia within the patches. After this, smaller unit cells show a more brittle behaviour, as already seen for the *static* case in Figure 4.1. For a better understanding of the dynamic behaviour of the different patches, again, 4×4 , 8×8 , and 12×12 unit cell patches are shown at 6%, 12% and 24% compression in Figure 4.4. As can be seen in the higher stress levels in Figure 4.3

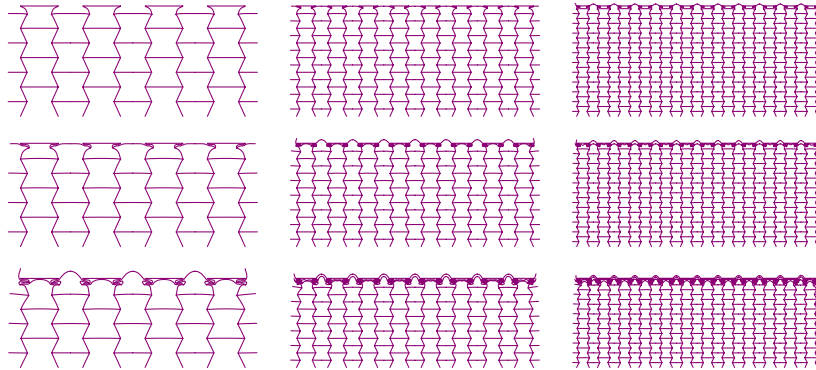


Figure 4.4: Re-entrant 4×4 (left), 8×8 (centre), and 12×12 (right) unit cell patches under *fast* rate deformation at 6%, 12% and 24% compression.

compared with Figure 4.1 and the concentration of the deformation near the moving boundary in the patches in Figure 4.4, the response is driven by inertia and not by the structural response. This is due to the fact that the accelerating forces are beyond the yield limit of the upper parts of the structure. These forces lead to a localized collapse of the structure near the strike face. The peaks observed throughout the stress-strain curves in Figure 4.3 put further emphasis on this observation. 6% compression corresponds with the first peak for the 8×8 unit cell patch, as indicated by the thin vertical line in Figure 4.3. At this compression level, it can be seen from Figure 4.4 that the first half unit cell is fully collapsed

and the corresponding horizontal row of beams starts to come into contact. The acceleration of this horizontal row of beams is the explanation for the increased stress experienced at the strike face. The size of half a unit cell in horizontal direction would correspond to 6.25% of the length for an 8×8 patch. The effect occurs already at lower compression levels due to the finite sized beams coming into contact already earlier. At 12% compression, showcased in the centre row of Figure 4.4, first contact can be seen for the 4×4 patch as well as contact with the second row of horizontal beams for the 8×8 patch. This corresponds well with the peaks in Figure 4.3. This observation provides a rationale for the earlier occurrence of peaks in the stress response for a smaller unit cell size. After a nominal compression of 24%, all deformation is concentrated at the top and the lower parts do not show any deformation. One should note here, that the bulging of the beams through the upper boundary is not an error, but a limitation of the employed boundary conditions only constraining the nodes at the top boundary in the undeformed configuration. The limitation is acceptable as the bulging elements are not causing numerical issues and are connected to the rest of the lattice. Furthermore, they are sufficiently far from the bottom boundary, which is the focus of the remaining investigations. The remaining stress-strain curves for *slow* and *medium* compression as well as the corresponding deformation patterns are shown in Appendix A.1.

4.2 Chiral unit cells

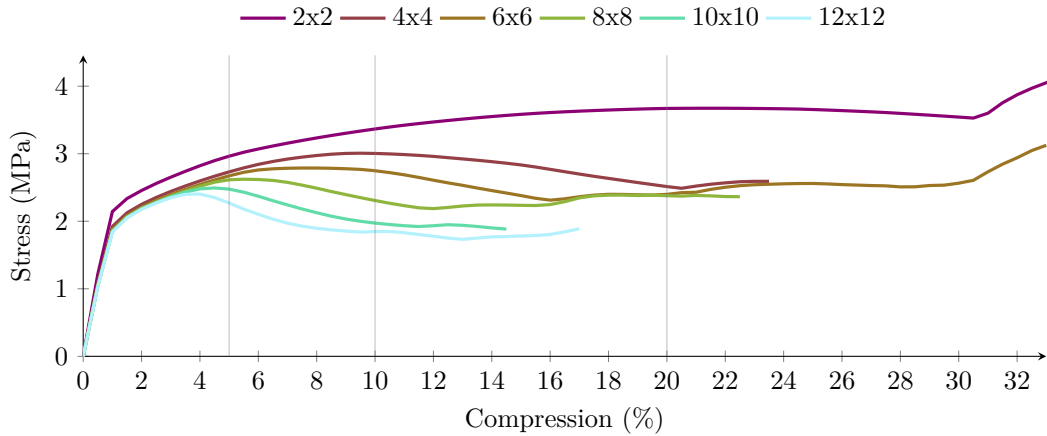


Figure 4.5: Stress-strain curves of patches with a different number of chiral unit cells under *static* compression.

Next to the re-entrant unit cell, the behaviour of patches from chiral unit cells is analysed. The *static* stress-strain curves are shown in Figure 4.5. Also for this architecture, in these curves the onset of plasticity can be seen at 1%. Similar to the re-entrant patches in Figure 4.1, all structures initially show a hardening response. This hardening response is then followed by a softening response, which is more pronounced for smaller unit cells. This is consistent with earlier observed tendencies, that smaller unit cells lead to an earlier and stronger localization of the deformation. The deformed configurations for 4×4 , 8×8 , and 12×12 patches at 5%, 10% and 20% are visualized in Figure 4.6. These compression levels are marked in Figure 4.5 by thin vertical lines. In the stress-strain curves, it can be seen, that at 5% compression both the 4×4 on the left and 8×8 patches in the centre are still in the first hardening phase, whilst the 12×12 patch on the right is already in the softening phase. Upon inspection of the deformation patterns, it can be seen, that the 12×12 patch exhibits localizations of deformation (near the top of the patch), whilst the other two still showcase uniform deformation. At 10% compression, the 12×12 patch on the right side of the figure shows contact, leading to a slightly stiffer response. The 8×8 patch in the centre has also entered the softening phase and showcases clearly localized deformation as well. The 4×4 patch on the left is near the peak of its stress level and when examining the deformation patterns, the start of localized deformation can be seen as well. At the last investigated compression level of 20%, the 8×8 patch shows multiple points of internal contact, which corresponds to the global hardening of the patch. On the other hand, the 4×4 patch shows no contact yet, which is consistent with the ongoing

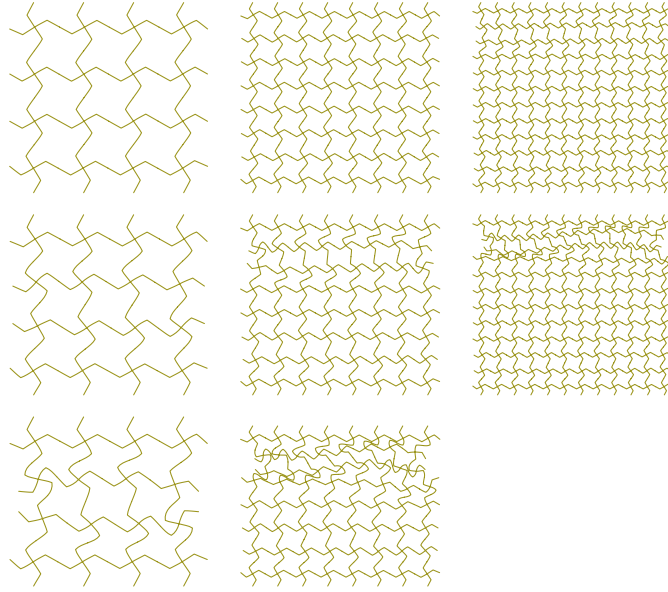


Figure 4.6: Chiral 4×4 (left), 8×8 (centre), and 12×12 (right) unit cell patches under *static* deformation at 5%, 10% and 20% compression.

softening behaviour of the overall patch as seen in Figure 4.5. After further deformation, beams within the patch will come into contact, marking the transition from the softening phase to the re-hardening phase. It should be noted, that chiral patches show strong local asymmetries in their behaviour despite the enforced global symmetry, due to the rotating mechanism responsible for the negative Poisson effect. For the chiral unit cells, as is the case for the re-entrant ones, the static solution scheme suffers from loss of convergence after a larger number of beams or the free ends of beams come into contact.

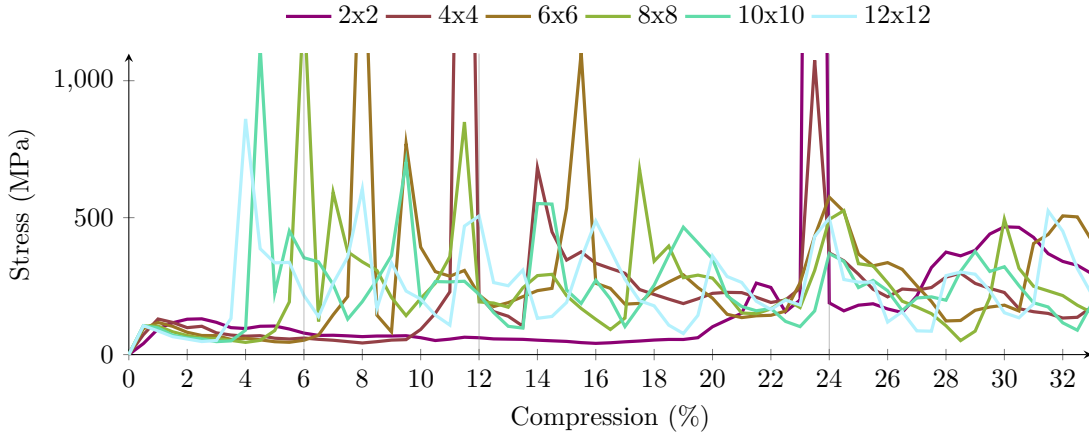


Figure 4.7: Stress-strain curves of patches with a different number of chiral unit cells under *fast* rate compression.

The dynamic behaviour is investigated for the chiral unit cells as well and the resulting stress-strain curves for *fast* compression are shown in Figure 4.7. An initial maximum appears around the onset of plasticity at 1% deformation. Here, as is the case for re-entrant patches, smaller unit cells show a stiffer response not seen in static deformation, attributed again to differences in the distribution of inertia within the patches. Furthermore, smaller unit cells show a more brittle response after the first peak around 1% compression, as seen earlier for the re-entrant unit cells in Figure 4.3, consistent with the *static* behaviour of both auxetic unit cells. Afterwards all investigated patches show further peaks, appearing later for larger unit cells, i.e. patches with a smaller number of unit cells. In order to understand

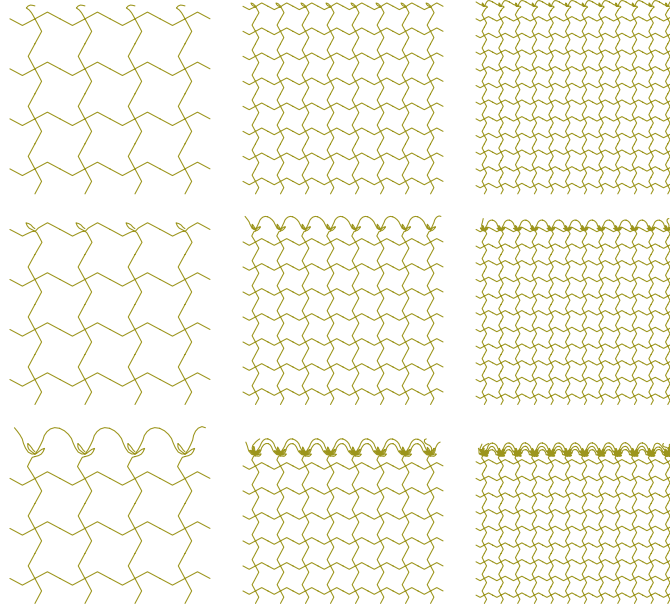


Figure 4.8: Chiral 4×4 (left), 8×8 (centre), and 12×12 (right) unit cell patches under *fast* rate deformation at 6%, 12% and 24% compression.

the reason behind these peaks, the deformed patches are plotted for 6%, 12% and 24% compression and shown in Figure 4.8. All patches show a clear localization of the deformation at the top and no deformation of the remaining parts of the structure. At 6% deformation, for the 8×8 patch, half a unit cell is compressed, and contact between the upper nodes as well as the next horizontal row of beams is achieved. The acceleration of these beams corresponds with a peak in the stress-strain curve seen in Figure 4.7. The same phenomenon can be seen in the 4×4 patch at 12% deformation, both in the deformation plots in Figure 4.8 and the stress-strain curve in Figure 4.7. The peaks are cut off in the figure for better visibility, but larger elements show peaks of higher magnitude, i.e. from the peak for 12×12 unit cells at about 800 MPa the stress level rises over approximately 2000 MPa for 6×6 unit cells to roughly 6000 MPa for the 2×2 unit cell patch. These phenomena are similar to the ones observed in the re-entrant patch. Additional stress-strain curves for *slow* and *medium* compression as well as the corresponding deformation patterns are shown in Appendix A.2.

4.3 Honeycomb unit cells

In order to make a comparison with the auxetic unit cells, regular honeycomb unit cell patches with a positive Poisson's ratio are investigated. The corresponding static stress-strain curves are shown in Figure 4.9. We observe the same kink in the curve at the onset of plasticity as for the patches with re-entrant and chiral unit cells. For smaller unit cells neither the reduction in the hardening response, observed for the re-entrant architecture, nor earlier softening, as for the chiral architecture, is observed. This is also confirmed in the deformation patterns of 4×4 , 8×8 , and 12×12 unit cell patches in Figure 4.10. Global barrelling is clearly visible for the 8×8 and 12×12 cases, in the centre and on the right side respectively. As the barrelling response is a global pattern we can, in Figure 4.9, observe a convergence of the response already at smaller numbers of unit cells compared to the two investigated auxetic structures in Figures 4.1 and 4.5, in which localized deformation is occurring.

For the dynamic investigation of different honeycomb patches, again the stress-strain curves under *fast* compression are examined, as shown in Figure 4.11. The initial response, prior to the onset of plasticity at 1% shows, opposed to the observations in static deformation, a stiffer response for smaller unit cells, motivated again by differences in the distribution of inertia for different sizes of unit cells. After this onset of plasticity, a more brittle response is observed for smaller unit cells, in agreement with the observations made for both auxetic architectures. In the stress-strain curves, peaks are seen at lower compression for smaller unit cells and at higher compression levels for larger unit cells as already seen in

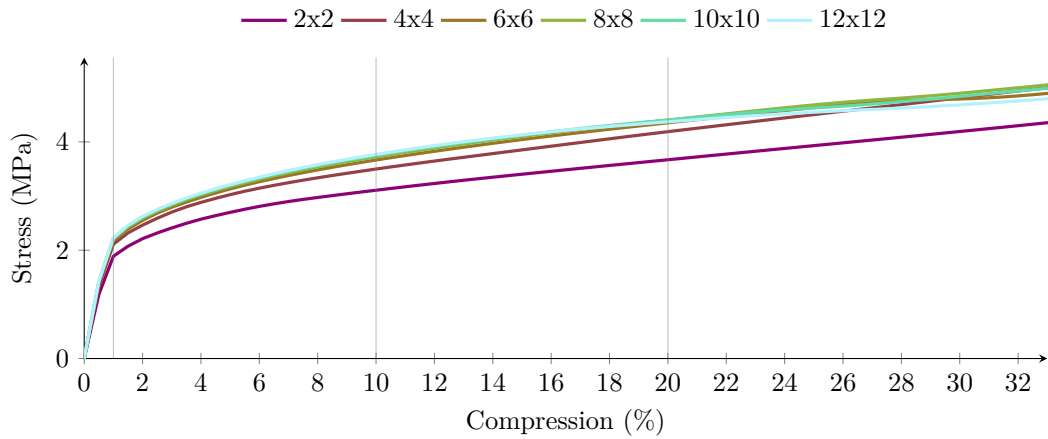


Figure 4.9: Stress-strain curves of patches with a different number of honeycombs unit cells under *static* compression.

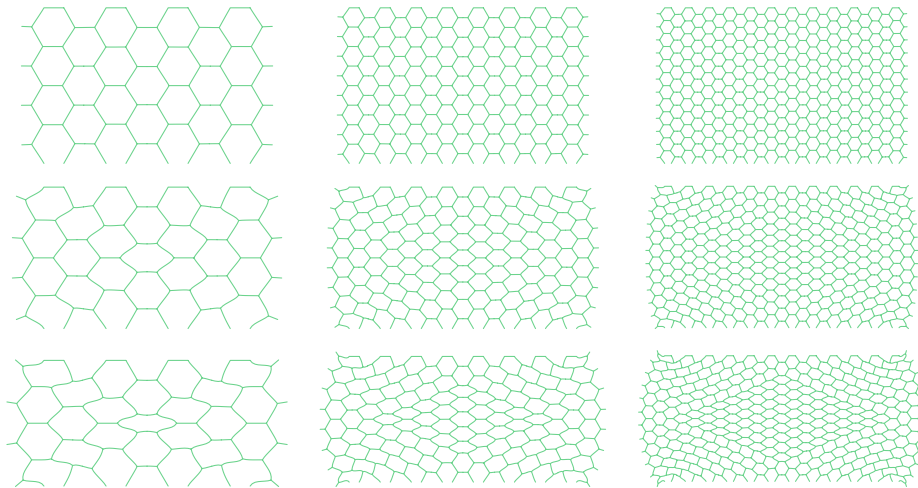


Figure 4.10: 4×4 (left), 8×8 (centre), and 12×12 (right) unit cell patches under *static* deformation at 1%, 10% and 20% compression.

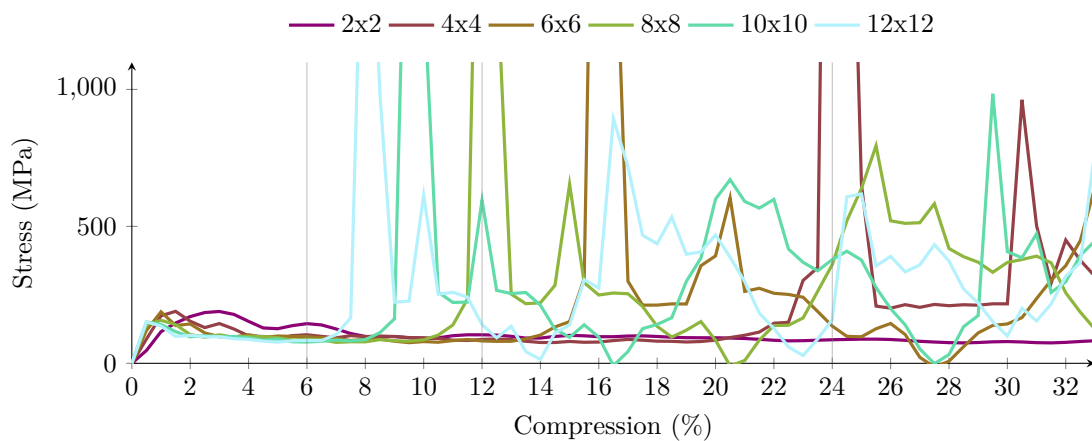


Figure 4.11: Stress-strain curves of patches with a different number of honeycombs unit cells under *fast* rate compression.

the responses of the two auxetic architectures. Nevertheless, fewer peaks are observed than for the two auxetic architectures. To illustrate the reason behind this, in Figure 4.12, the deformed shapes of 4×4 ,

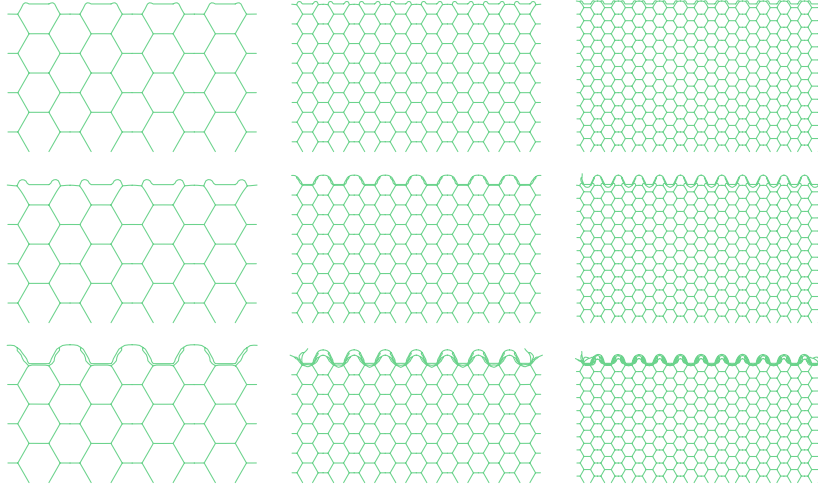


Figure 4.12: 4×4 (left), 8×8 (centre), and 12×12 (right) unit cell patches under *fast* rate deformation at 6%, 12% and 24% compression.

8×8 , and 12×12 unit cell patches at compression levels of 6%, 12% and 24% are shown. Whereas both auxetic structures show peaks in their stress response at a compression level of 6%, this peak is not seen in the response of the non-auxetic patches. In the deformed shapes in Figure 4.12, it can be seen, that none of the patches show any contact yet, as the beams at the upper boundary do not come into contact with the beams at half a unit cell height due to the convex structure of the honeycomb architecture. For this same reason, a full unit cell of compression is needed for the non-auxetic honeycomb structures to experience contact. At this point, shown in the centre row at 12% compression for the 8×8 patch in the central columns and in the bottom row at 24% compression for the 4×4 patch on the left side, contact is seen. This corresponds with the stress peaks in Figure 4.11, where the first peak for the 8×8 patch occurs at 12% and the first peak of the 4×4 patch at 24%. These values are again marked by thin vertical lines. For better readability of the graph, the peaks are again cut off but are rising from about 2000 MPa for the 12×12 patch up to about 4000 MPa for the 4×4 patch. The 2×2 unit cell patch does not show a peak in the first 33% compression. The other stress-strain curves for *slow* and *medium* compression as well as the corresponding deformation patterns are shown in Appendix A.3.

4.4 Comparison of unit cells

Balancing the convergence behaviour in the *static* case, the dynamic behaviour and the computational cost, it is decided to take 8×8 unit cell patches as representative. Thus, 8×8 patches are used in the dynamic investigations in Sections 5 and 6 on force transmission and energy distribution.

A first comparison between 8×8 patches using the three architectures is shown in Figure 4.13. In this figure, the stress-strain curves are shown for the investigated rates. During *static* compression, both investigated auxetic architectures, re-entrant and chiral, show a similar level of stress, whereas the honeycomb architecture not only shows a higher overall level, but also a significant hardening throughout the compression. This difference is explained by the fundamentally different deformation modes in the patches: localized collapse in the case of the re-entrant and chiral architectures versus global barrelling in the case of the honeycomb. Also for *slow* compression, the honeycomb shows higher stress levels at the strike face compared to the auxetic architectures. As the *static* deformation patterns are less relevant at higher speeds, in the *medium* rate, peaks begin to appear, as discussed above. Here the re-entrant structure remains at a low stress level, and both the chiral and honeycomb patches show a large fluctuation of similar magnitude. This is even further emphasized for the *fast* rate, where the chiral and honeycomb structures again exhibit peaks of comparable magnitude, with the re-entrant patch remaining at a lower stress level, despite a few distinct peaks. From this it can be concluded that in all loading scenarios, the honeycomb structure outperforms the auxetic ones regarding the stress needed to

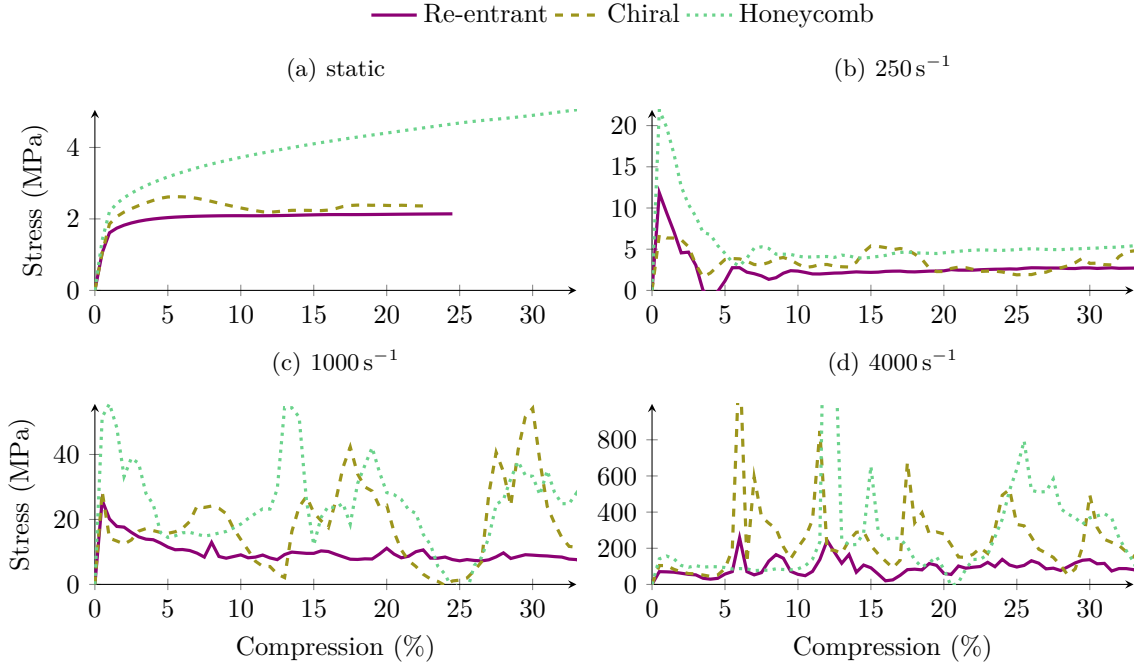


Figure 4.13: Comparison of the stress-strain curves at the strike face for 8×8 patches of different architectures for the four investigated strain rates.

compress the patch to the same level. For all investigated architectures, whilst the *static* deformation modes differ and only the auxetic patches show localized deformation, during *fast* compression, the response is dominated by inertial effects, leading to a more brittle behaviour for smaller unit cells of all architectures, as discussed in the previous sections. Dynamic effects within the patches will be investigated in more detail in the following.

5 Effects of strain rate on the force transmission

In order to assess the efficacy of a protection concept, one not only needs to assess the forces exhibited at the strike face, but also the transmission of those forces through the protective layer, as was done in [15] for an emulated impact event with focus on the local distribution of these forces. The measurement of the forces acting on the strike face during an impact event has little information regarding the forces acting on the back face, thus the next investigation focuses on the transmission of forces from the strike face to the back face.

5.1 Re-entrant patch

To investigate this transmission of the force through the protective layer, a first comparison is done between the stresses on the strike face and the back face for the *slow* rate compression. The corresponding stresses, both on the strike face (the top boundary in Figure 3.1) and on the back face (the bottom boundary in Figure 3.1), are shown over the compression in Figure 5.1. An additional abscissa is given depicting the time corresponding to the amount of compression at this strain rate. The stress on the back face follows the stress on the strike face with a delay, and both finally converge towards the same stress level. The magnitude of the delay, especially in the first rise of the stress, can be explained by the time needed for the elastic pressure wave to travel through the patch. Given the material parameters laid out in Section 3, the pressure wave speed through a beam is

$$c_{\text{metal}} = \sqrt{\frac{210 \text{ GPa}}{7850 \text{ kg m}^{-3}}} \approx 5172 \text{ m s}^{-1}. \quad (8)$$

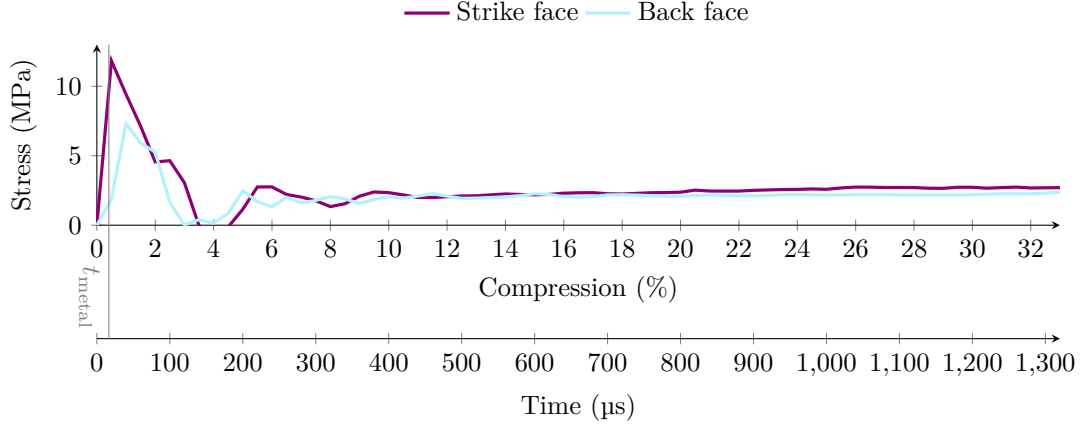


Figure 5.1: Comparison of the stress on the strike face and the back face under *slow* compression for an 8×8 re-entrant patch.

Together with the height of the patch of $h = 77.7$ mm and the angle between the beams and the vertical of $\alpha = 24.4^\circ$, the time required for the pressure wave to reach the bottom equals

$$t_{\text{metal}} = \frac{h/\cos(\alpha)}{c_{\text{metal}}} \approx 16.5 \mu\text{s}. \quad (9)$$

This time is marked in Figure 5.1 with a thin vertical line and corresponds with the first rise in stress being recorded at the back face.

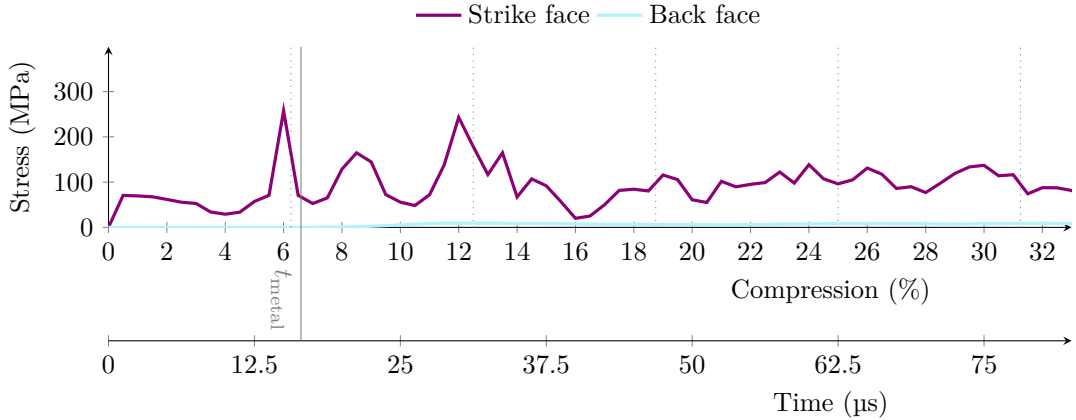


Figure 5.2: Comparison of the stress on the strike face and the back face under *fast* compression for an 8×8 re-entrant patch.

The behaviour of the patch under *fast* rate compression is then investigated, and the resulting stresses recorded at the strike face and the back face are shown in Figure 5.2. The delay in the stress on the back face is again visible and corresponds with the time required for the stress wave through the metal t_{metal} . In this graph, the peaks in the stresses on the strike face at intervals of 6.25%, corresponding to half the height of a unit cell, as discussed in Section 4 can be seen as well.

To compare different rates, in Figure 5.3, the stresses on both faces are plotted for the investigated compression rates. On the strike face, we can observe an increase of the stresses needed to compress the patch at the given rates. This increase is moderate for *slow* and *medium* rate compression when compared to *static* compression, but increases significantly for *fast* rate compression. On the back face, it is clearly observed, that the stresses for both *slow* and *medium* rate compression approach *static* compression stress, despite the increase seen on the strike face. For the *fast* compression case, this cannot be observed. The increase seen here between the different compression rates is however

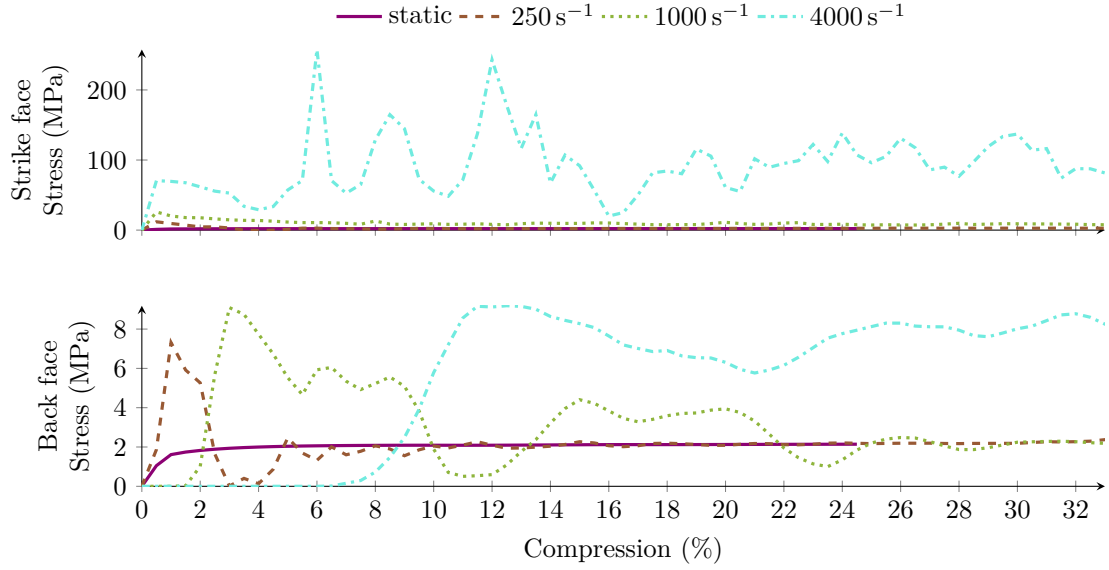


Figure 5.3: Stresses on both faces for the re-entrant patch for different compression rates.

small, when compared to the increase in stresses on the strike face, leading to the assumption, that the stress transmitted to the back face, after an initial peak, is in a first approximation independent of the compression rate. These initial peaks show similar magnitudes irrespective of the compression rate. The stresses transmitted to the back face are reduced when compared to the stress experienced at the strike face. This is mostly due to an increase in the dynamic stresses at the strike face, whilst the stresses at the back face have about the same magnitude. The mechanisms of dissipation of these forces will be discussed in Section 6. Plots comparing the stresses at the strike face and the back face for *static* and *medium* rate compression can be found in Appendix B.1.

5.2 Chiral patch

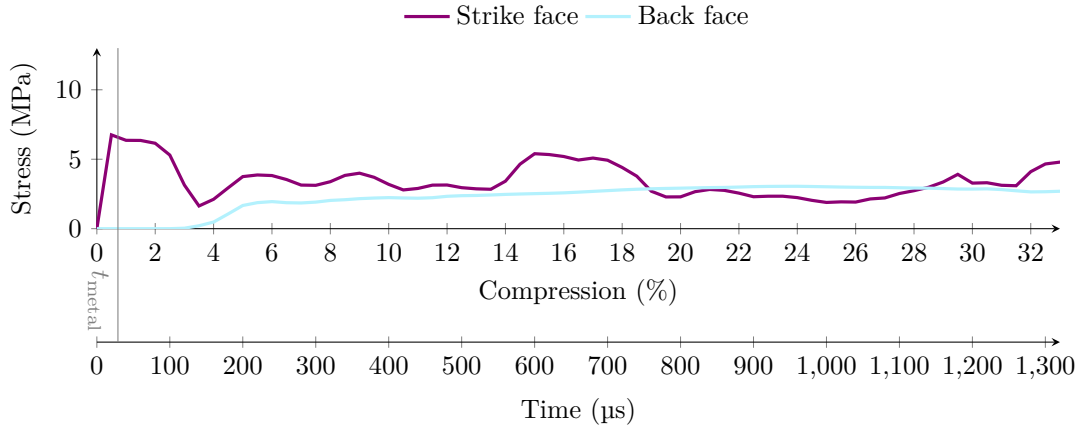


Figure 5.4: Comparison of the stress on the strike face and the back face under *slow* compression for an 8×8 chiral patch.

Next to the re-entrant architecture also the dynamic effects in the chiral architecture are investigated. The stresses on both faces for *slow* compression are shown in Figure 5.4. In this figure, the stresses are plotted over both the compressive strain, and the corresponding time. As for the re-entrant case, the theoretical time needed for a pressure wave travelling through a beam $t_{\text{metal}} \approx 28.9 \mu\text{s}$ is indicated by a vertical line. This time is different from the re-entrant patch due to a different geometry (more

explanation given in Appendix B.2). It can be seen in Figure 5.4, that the pressure wave reaches the bottom significantly later than would be expected by a wave travelling unhindered through a metal beam. This is attributed to the impedance jumps at the sharp kinks in the chiral unit cell, leading to partial reflection and conversion from pressure to shear waves. Similar to the re-entrant patch, also for the chiral patch, the stress on both faces converge towards the same value. This convergence is slower than for the re-entrant patch, which is consistent with the longer times required for the stress waves to transverse the patch.

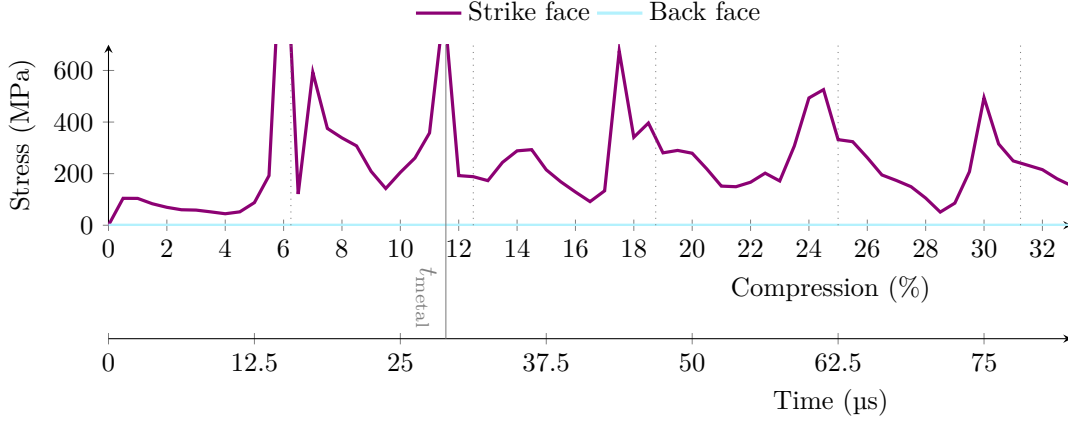


Figure 5.5: Comparison of the stress on the strike face and the back face under *fast* compression for an 8×8 chiral patch (the values of the peaks outside the figure axis are approximately 1250 MPa at 6% compression and approximately 800 MPa at 11.5% compression).

In Figure 5.5 the stresses for *fast* compression of the chiral patch are depicted. The peaks can again be attributed to the acceleration of horizontal rows of beams at half unit cells. A delay of the pressure waves reaching the bottom of the patch, as discussed above for *slow* compression, can be seen again for the *fast* compression case. The point where the stress on the back face starts to be observable is well beyond the plotted range of $82.5 \mu\text{s}$. Prior to this, stress on the back face is insignificant at well below 1 MPa.

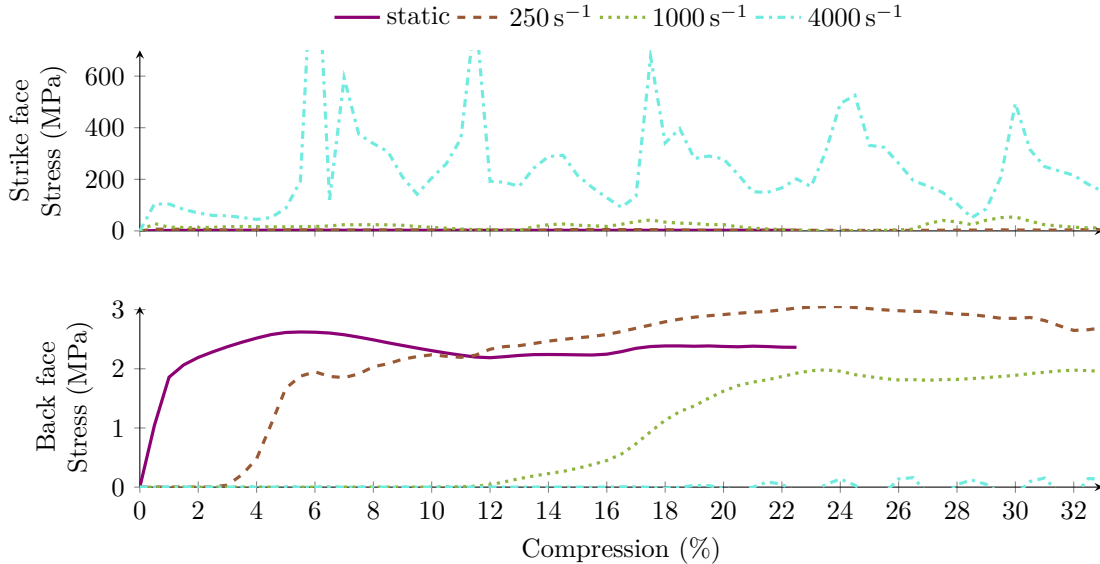


Figure 5.6: Stresses on both faces for the chiral patch for different compression rates.

In order to get a better estimation of the effect different strain rates have on the response of the chiral patch, the stresses on both faces for different strain rates are compared in Figure 5.6. As is the

case for the re-entrant patch, the chiral patches show an increase of stress needed for the compression of the patch at the strike face with an increase in rate. This increase is moderate for *slow* and *medium* rate compression, and again significantly more pronounced for the *fast* rate. The stresses on the back face are less evidently approaching a common value as is the case for the re-entrant patch. Although the compression at *static*, *slow*, and *medium* rates seem to converge towards the same value, a longer time interval is needed in order to assess this effect in more detail. This longer time interval is also needed to be able to give an indication on the effects of the *fast* compression onto the stresses seen at the back face, as the pressure waves through the material need more time to reach the back face of the patch. This longer time interval relates to higher compression, which results in densification and thus a response more akin to a solid material and no longer a heterogeneous metamaterial. At this stage of densification, the formulation of the contact stiffness reaches a limit as well, and a more sophisticated modelling of the contact would be required. It is thus opted not to conduct these simulations. Plots comparing the stresses at the strike face and the back face for *static* and *medium* rate compression can be found in Appendix B.2.

5.3 Honeycomb patch

The behaviour of non-auxetic honeycombs under dynamic compression is investigated as well. The

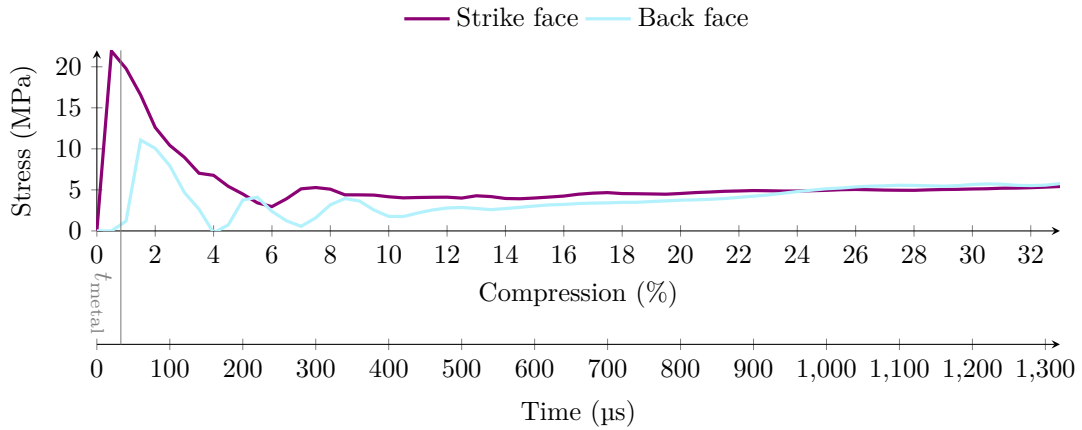


Figure 5.7: Comparison of the stress on the strike face and the back face under *slow* compression for an 8×8 honeycomb patch.

stresses on the strike face and back face for the honeycomb patches, at *slow* rate compression, can be seen in Figure 5.7. The time for the pressure wave to propagate through the metal $t_{\text{metal}} \approx 32.9 \mu\text{s}$ is indicated by a vertical line (see Appendix B.3). The general behaviour of the honeycomb unit cell patch, does not deviate from the auxetic unit cell patches. The time delay for the stresses at the back face to rise roughly corresponds with the metal wave speed. Later on stresses on both the front and strike face converge towards a common plateau.

The behaviour of the honeycomb patch for the *fast* rate compression, as seen in Figure 5.8, shows again lower stresses on the back face compared to the stresses on the strike face. This is consistent with the observations for the auxetic patches.

For a better understanding of the strain rate effect in the non-auxetic patch, the stresses on both faces are shown for the different investigated strain rates in Figure 5.9. As with the auxetic patches, we can see the stress on the back face for *slow* compression approaching the stress level for the *static* compression. The stress for *medium* compression shows large oscillations around the same level as well. Finally, at *fast* compression, the stress appears to be higher, which is in agreement with the observations made for the auxetic unit cells. This increase is however negligible when compared to the increase in stress at the strike face. A much higher increase in stress on the strike face is needed to compress the patch at the *fast* rate compared to the *medium*, *slow*, and *static* compression cases, which is seen in the auxetic patches as well. Plots comparing the stresses at the strike face and the back face for *static* and *medium* rate compression can be found in Appendix B.3.

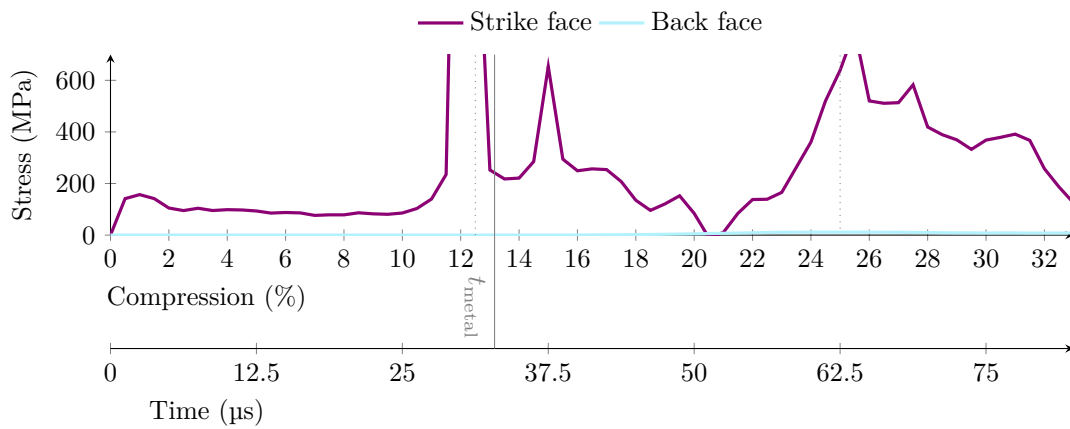


Figure 5.8: Comparison of the stress on the strike face and the back face under *fast* compression for an 8×8 honeycomb patch (the values of the peaks outside the figure axis are approximately 2500 MPa at 12% compression and approximately 900 MPa at 25% compression).

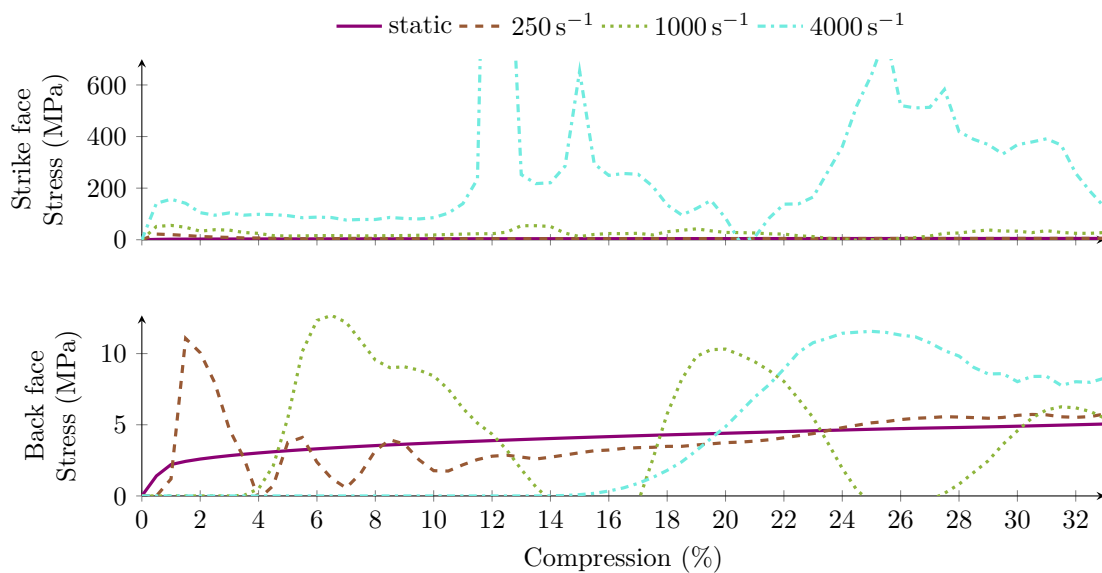


Figure 5.9: Stresses on both faces for the honeycomb patch for different compression rates.

5.4 Comparison of patches

Summarizing the findings of this section, two observations can be made: Firstly, that the speed of the pressure waves through the metal is a lower bound for the stress to reach the back face. This theoretical phenomenon can also be observed in the simulations. This lower bound is approached when more straight beams and fewer kinks and joints are present within an architecture, resulting the chiral patch in a significant delay after the theoretical lower limit. Secondly, the stress amplitudes experienced at the back face appear to be largely unaffected by the strain rate. The peak stresses experienced in all investigated rates can be regarded as equivalent, and the final, constant stress level approaches the static compression value for all investigated structures. However, this is only a first approximation; a full understanding of the impact protection effect of the different patches requires the consideration of the force-time record and subsequent effects on the protected material.

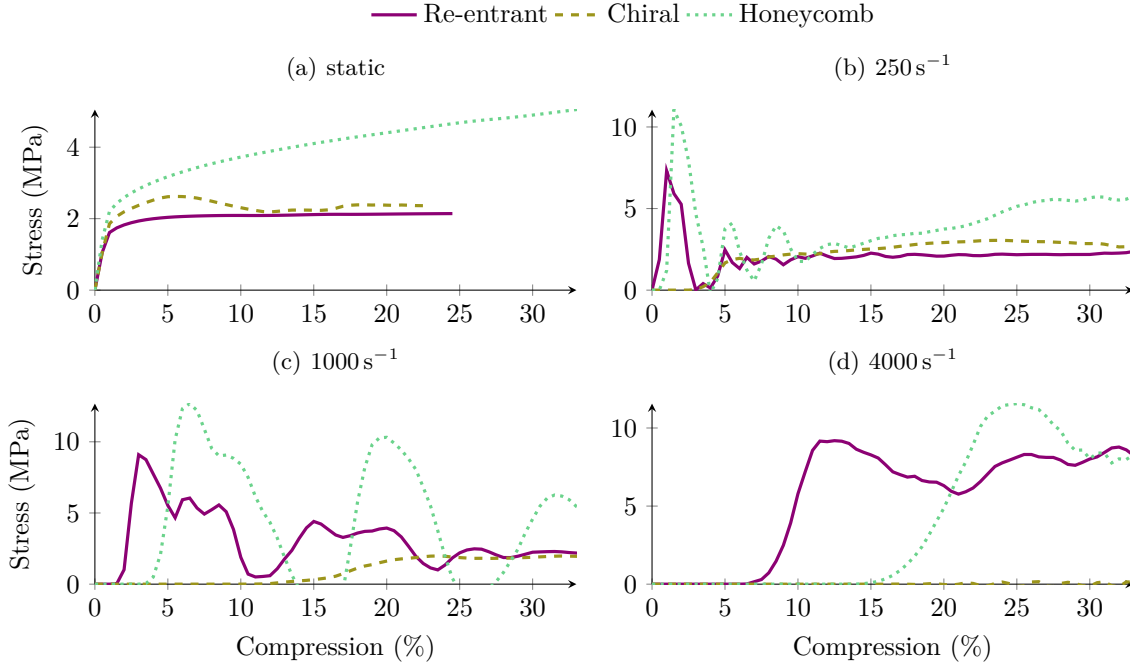


Figure 5.10: Comparison of the stresses at the back face for 8×8 patches of different architectures for the four investigated strain rates.

Both observations can also be seen by comparing the stress curves at the back face of the three patches in Figure 5.10. In this figure, the first effect is clearly observable as the rise in stress level appears later for patches with less straight connections between the top and the bottom. For instance, both the re-entrant and the honeycomb unit cell can be considered. The beams of the re-entrant patch are 24.4° off the vertical, whereas the beams for the honeycomb patch are 29.7° off, meaning the re-entrant patch offers a more straight vertical line for the pressure waves to the bottom compared to the honeycomb patch. The angle is however not the only factor for the time of the waves reaching the back face, as can be seen by the much later rise in stress for the chiral patch, of which the beams are only 28.1° off the vertical, but exhibit more kinks and joints when compared to the other two architectures. The chiral architecture contains beams meeting in 90° angles at their joints, amplifying this effect. Comparing the stress levels at the back face between the architectures, *static* compression shows the same graph as the strike face, resulting in Figure 5.10a being identical to Figure 4.13a. Considering higher compression rates, the chiral architecture appears to show the lowest stress levels at the back face, despite showing similarly high stress levels at the strike face compared to the honeycomb structure. This observation is based on the *slow* and *medium* compression rates, as in the *fast* compression rate, the stress does not reach the back face for the chiral patch within the investigated time, however a qualitatively similar result is to be expected. These results indicate the chiral architecture as a good candidate for impact mitigation.

6 Local energy distributions

In order to facilitate a more thorough understanding of the mechanisms exhibited in the previous section, the SEA, as defined by Equation (7) spent on compression of the patches and its subsequent distribution into various components of energy throughout the patches is analysed. For the present analyses, the global specific energy is split into elastic potential energy, inelastic dissipated energy, and kinetic energy. The spatial distribution of the elastic, dissipated, and kinetic energy measures over the two directions of the patch, based on the nodal energy levels as explained in Section 3, will be analysed as well.

6.1 Re-entrant patch

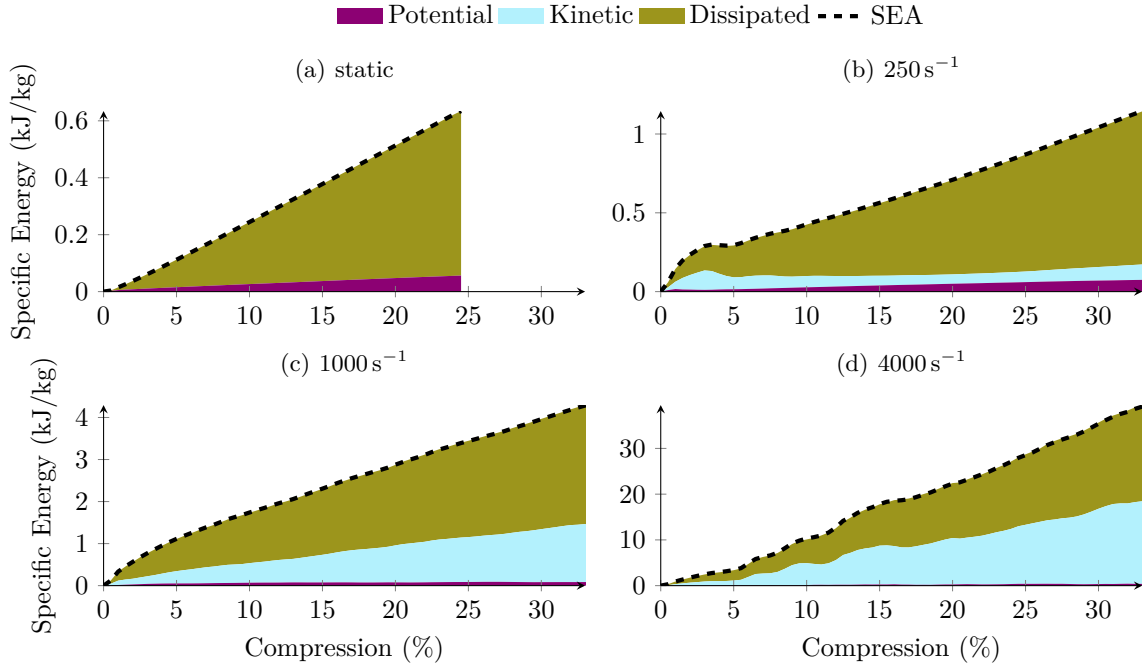


Figure 6.1: Distribution of the SEA into different types of energy for the 8×8 re-entrant patches at different strain rates.

The first comparison is the distribution of energy in the patch at different compression rates shown in Figure 6.1 for the re-entrant patch. In Figure 6.1a, *static* deformation is shown. At around 1%, plastic deformation starts to occur, which coincides with the loss in stiffness seen in Figure 4.1. During the remainder of the analysis, the majority of the SEA put into the system is dissipated through plastic deformation, and only a minor increase in elastically stored potential energy can be observed. This increase can be related to the hardening present in the material model. In Figure 6.1b, the distribution of energy for *slow* compression is shown. The ratio between dissipated and potential energy remains roughly the same and the kinetic energy contributes only a minor part to the total SEA spent on compressing the material. In Figure 6.1c, the distribution of energy in the *medium* compression scenario is shown. While the dissipated energy is still the dominant form of energy present in the system, the amount of kinetic energy increases whilst the potential energy vanishes. This effect is visible in a more pronounced way in Figure 6.1d, showing both contributions of the kinetic and dissipated energy being at similar levels. Note, that the force peaks observed in Figure 5.2, can be seen in the energy plots as well. At the half unit cell points—at multiples of 6.25%—the kinetic energy shows a sharp increase.

Next to the distribution of energy for different physical mechanisms, the distribution of energy across the lattice structure is investigated. In Figure 6.2, the deformation after 20% *static* compression is depicted with marginal distributions of the energy density split into the different physical mechanisms shown at the top and the right of the patch. While the symmetry between the left and the right side remains intact, the top-bottom symmetry is broken by the more localized deformation near the bottom.

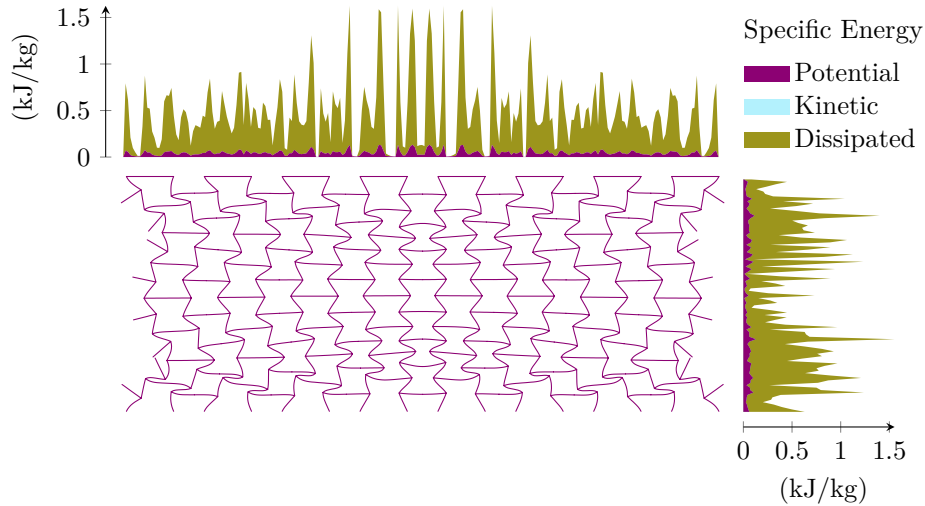


Figure 6.2: Local distribution of energy at 20% compression for *static* compression of the 8×8 re-entrant patch.

The plastic nature of this collapse is emphasized by a higher specific dissipated energy near the bottom of the patch.

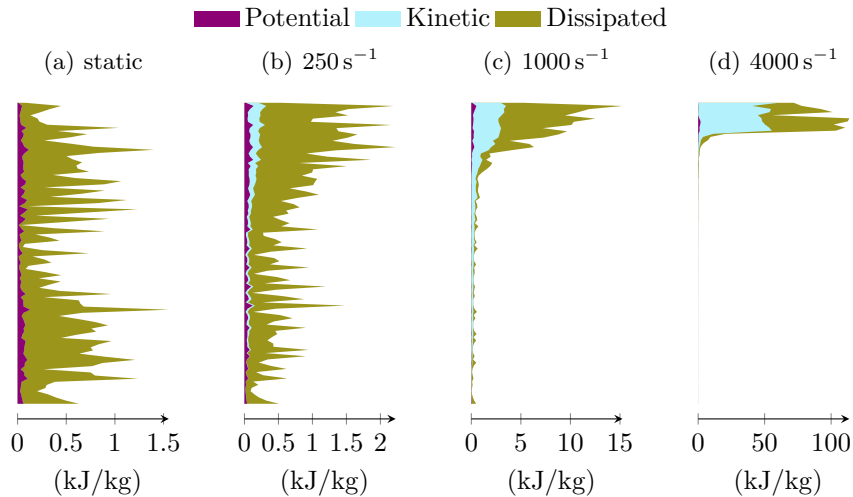


Figure 6.3: Vertical distribution of energy at 20% compression for all investigated compression rates in the 8×8 re-entrant patch.

In Figure 6.3 the vertical distribution of the absorbed energy is shown for the four investigated rates. Comparing the *static* results to the *slow* rate compression case, in Figures 6.3a and 6.3b respectively, confirms the observation from Figure 6.1, that the dissipated energy is responsible for the majority of the SEA needed to compress the patch. Only a minor portion of the SEA is stored in potential energy, and at *slow* compression, the kinetic energy contributions are of course comparatively small. A shift of the energy distributions towards the strike face at the top of the patch is however observed. This shift in the distributions can be seen more pronounced in Figure 6.3c for the *medium* rate, where the dissipated energy still takes up the majority of SEA, as discussed above. At *medium* compression, although the bulk of the energy is dissipated near the top, still a significant part of the energy is present in the lower parts of the patch. This is no longer the case for the *fast* compression rate seen in Figure 6.3d. For this rate, the amounts of energy seen at the lower parts of the structure appear negligible, and the energy distributions show a clear increase in the relative share of kinetic energy, which is in agreement with

the observations from Figure 6.1. This negligible amount of energy in the lower parts of the structure is in agreement with the deformation patterns shown in Figure 4.4. As discussed above, the deformations remain small in the lower parts of the patch at this *fast* rate, as also can be seen by the lack of lateral contraction at the boundaries, that would be expected from the negative Poisson's ratio of this structure, resulting in negligible amounts of energy in the lower parts of the patch.

6.2 Chiral patch

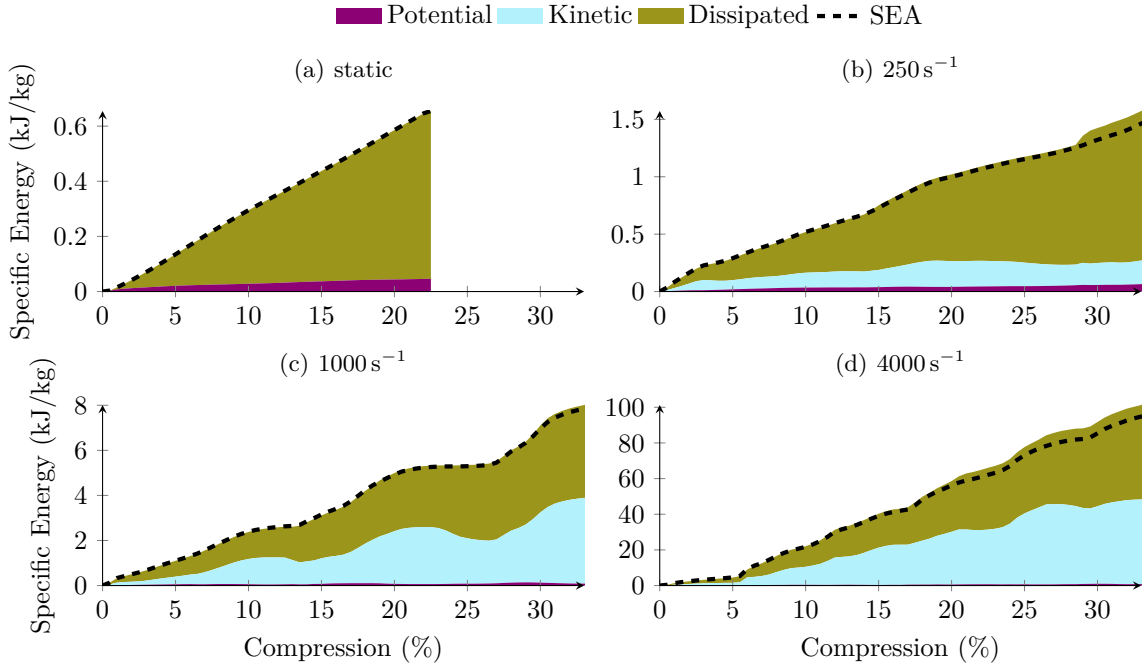


Figure 6.4: Distribution of the SEA into different types of energy for the 8×8 chiral patches at different strain rates.

The energy distribution in the chiral patch under different deformation rate is analysed in the same manner. In Figure 6.4, the distribution of the SEA in potential, kinetic, and dissipated energy is shown for different rates. The observations made for the re-entrant patch hold for the chiral patch as well. At *static* deformation, the majority of the SEA spent on compressing the material is dissipated throughout the deformation and only a minor increase in potential energy due to hardening of the material can be seen. At higher strain rates, the total SEA increased, as well as the share of kinetic energy. The share of kinetic energy at the *medium* rate is already half of the total energy, whereas for the re-entrant patch, this only happens at the *fast* rate, indicating an increased rate sensitivity of the chiral lattice. The higher sum of the different forms of specific internal energy compared to the externally computed SEA seen in Figures 6.4b and 6.4d is due to interpenetration of singular beams, that lead to divergence in the *static* case (Figure 6.4b) and represent an unphysical source of energy in the dynamic simulations. Since this effect is small and does not influence the global behaviour of the lattice, it is deemed acceptable.

The strain rate sensitivity of the chiral patch, can also be seen when comparing the vertical distributions of energy in Figure 6.5. In this figure, the vertical distribution of energy throughout the patch is plotted for the four investigated rates. In Figures 6.5c and 6.5d, depicting the *medium* and *fast* rate compression, the complete concentration of energy at the top is shown. This is consistent with the observations made in Figure 6.4 and further emphasizes the increased strain rate sensitivity of the chiral architecture when compared to the re-entrant architecture. The chiral patch at *low* rate compression, shows a similar trend compared to the re-entrant patch. A small shift of energy towards the top can be observed, with the energy in lower parts being more uniformly distributed. A similar shift of energy towards the top can be observed in *static* compression in Figure 6.5a, this is however explained by the localized deformation in singular rows of unit cells, as shown in Figure 4.6, where the deformation cor-

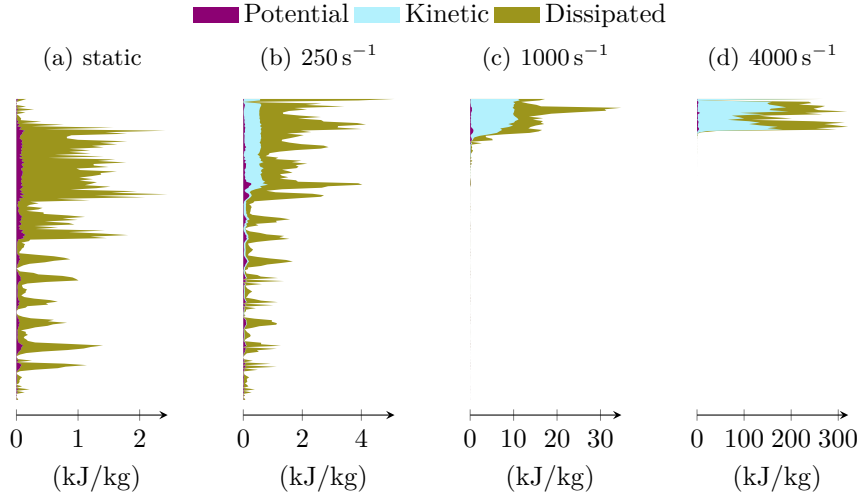


Figure 6.5: Vertical distribution of energy at 20% compression for all investigated compression rates in the 8×8 chiral patch.

responding to this distribution is shown for the 8×8 patch at 20% compression. The localization of deformation around the unit cells corresponds with a significant increase in energy dissipated and only a minor increase in elastically stored energy, as shown in Figure 6.5a.

6.3 Honeycomb patch

Finally, the distribution of energy in the honeycomb patch is investigated. In Figure 6.6, the different forms of energy are again compared for *static*, *slow*, *medium* and *fast* rates of compression. Here, the phenomena observed in the re-entrant and chiral patch, can be seen as well. The majority of the energy is dissipated and the fraction of kinetic energy rises with increasing compression rate. Two observations are noteworthy: Firstly, the peaks in force on the strike face observed at *fast* compression, seen in Figure 5.8, correspond with the sudden rise of kinetic energy in Figure 6.6d as well. In Figure 4.12 the acceleration of horizontal bars is illustrated, leading to both force peaks and a fast rise in kinetic energy. Secondly, at *medium* rate compression, the kinetic energy takes less than half of the energy in the patch, resembling the behaviour of the re-entrant patch, distinct from the chiral patch. This is seen by the vertical distributions of energy in Figure 6.7 as well. Here, at *medium* rate, the energies are shifted to the upper boundary, but still a significant amount of energy is in the bottom part of the lattice, similar to the observations made for the re-entrant patch. This is no longer the case for the *fast* rate, where energy is fully concentrated at the upper part near the strike face. At *slow* compression, a nearly linear distribution of all energies rising from the bottom to the top can be seen, with more energy dissipated close to the strike face. *Static* compression shows a bulge in the centre of the patch, consistent with the global barrelling seen in Figure 4.10. The peaks near the top and the bottom of the distribution are attributed to the strong deformation of elements at the fixed boundaries.

6.4 Comparison of patches

There are two commonalities between different metamaterial architectures when considering the energy distributions. Firstly, the majority of energy spent on compressing the material is dissipated by plastic deformation of the material throughout all compression rates. At higher rates the amount of kinetic energy approaches the level of plastically dissipated energy in the patch. This corresponds to the second common effect at higher rates, noted in earlier sections. The behaviour is not determined by the transmission of forces, but rather by the inertial forces that result from the distribution of mass within the lattice.

For a fair comparison of the different architectures, the SEA is plotted against the compression for the three investigated architectures. In Figure 6.8a, the SEA can be seen for *static* compression.

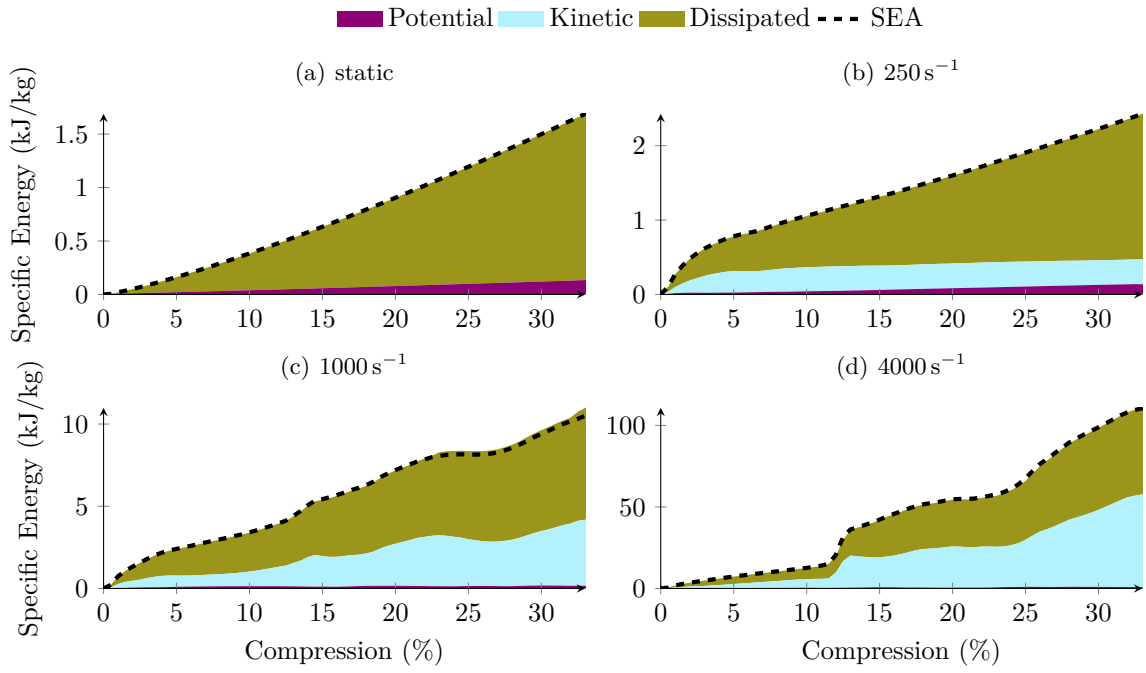


Figure 6.6: Distribution of the SEA into different types of energy for the 8×8 honeycomb patches at different strain rates.

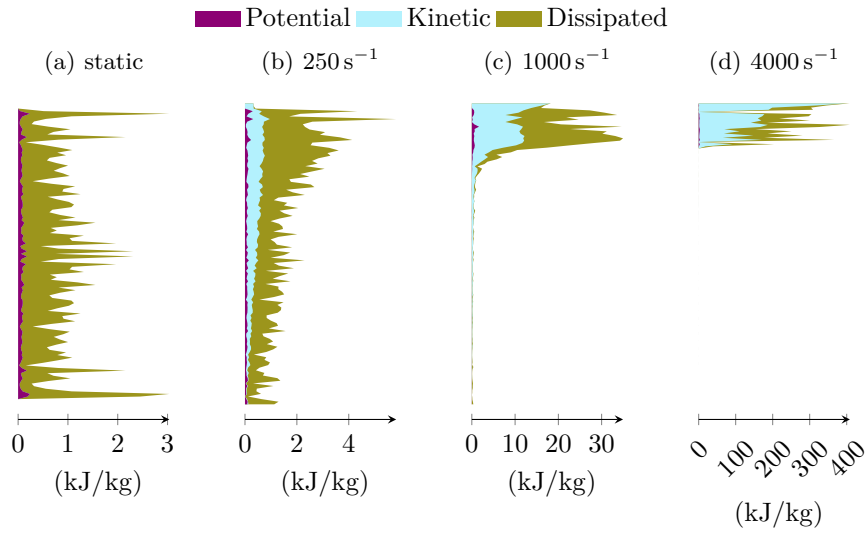


Figure 6.7: Vertical distribution of energy at 20% compression for all investigated compression rates in the 8×8 honeycomb patch.

of localized deformation is observed for the auxetic architectures, whereas for the globally barrelling honeycomb structure, the energy is more evenly distributed. At higher strain rates, the distribution of energy is concentrated at the top of the lattice near the strike face, consistent with the localized deformation patterns seen in Section 5. The chiral architecture shows the highest sensitivity to strain rate, whilst the honeycomb architecture shows the largest amount of SEA across the investigated cases.

Throughout this study no beneficial contribution from a negative Poisson's ratio for impact mitigation can be found. The obtained results allow designers of protection concepts to make an informed decision on the architecture and the size of the unit cells based on force transmission during static compression together with an estimation of the maximum force pulse during higher rate compression. Next to the practical applications, also new research avenues have been opened into impact resistant metamaterials away from simply auxetic structures towards architectures that focus on the limitation of the transmitted forces.

Author contributions

T. Gärtner: Conceptualization, Data curation, Investigation, Methodology, Software, Validation, Visualization, Writing - original draft **S.J. van den Boom:** Conceptualization, Methodology, Supervision, Writing - review & editing **J. Weerheijm:** Conceptualization, Funding acquisition, Writing - review & editing **L.J. Sluys:** Conceptualization, Funding acquisition, Methodology, Supervision, Writing - review & editing

Declaration of competing interests

The authors declare that they have no known competing financial interests or personal relationships that could have appeared to influence the work reported in this paper.

Acknowledgements

The project is financed by TNO through the PhD program of the Dutch Ministry of Defence. The authors acknowledge the use of computational resources of the DelftBlue supercomputer, provided by Delft High Performance Computing Centre (<https://www.tudelft.nl/dhpc>) [12]. The availability of scientific colour maps [8] used in this publication is highly appreciated.

Data availability

The code employed for conducting the finite element analyses in this contribution is available on GitHub.

References

- [1] I. I. Argatov, R. Guinovart-Díaz and F. J. Sabina. 'On local indentation and impact compliance of isotropic auxetic materials from the continuum mechanics viewpoint'. In: *International Journal of Engineering Science* 54 (2012), pp. 42–57.
DOI: 10.1016/j.ijengsci.2012.01.010
- [2] R. P. Bohara et al. 'Anti-blast and -impact performances of auxetic structures: A review of structures, materials, methods, and fabrications'. In: *Engineering Structures* 276 (2023).
DOI: 10.1016/j.engstruct.2022.115377
- [3] S. Bonfanti et al. 'Computational design of mechanical metamaterials'. In: *Nat Comput Sci* 4.8 (2024), pp. 574–583.
DOI: 10.1038/s43588-024-00672-x

- [4] C. R. Calladine and R. W. English. ‘Strain-rate and inertia effects in the collapse of two types of energy-absorbing structure’. In: *International Journal of Mechanical Sciences* 26.11-12 (1984), pp. 689–701.
DOI: 10.1016/0020-7403(84)90021-3
- [5] J. B. Choi and R. S. Lakes. ‘Fracture toughness of re-entrant foam materials with a negative Poisson’s ratio: experiment and analysis’. In: *International Journal of Fracture* 80.1 (1996), pp. 73–83.
DOI: 10.1007/bf00036481
- [6] J. B. Choi and R. S. Lakes. ‘Non-linear properties of metallic cellular materials with a negative Poisson’s ratio’. In: *Journal of Materials Science* 27.19 (1992), pp. 5375–5381.
DOI: 10.1007/bf02403846
- [7] C. Coulais, C. Kettens and M. van Hecke. ‘A characteristic length scale causes anomalous size effects and boundary programmability in mechanical metamaterials’. In: *Nature Physics* 14.1 (2017), pp. 40–44.
DOI: 10.1038/nphys4269
- [8] F. Cramer. *Scientific colour maps*. Version 8.0.1. Oct. 2023.
DOI: 10.5281/zenodo.8409685
- [9] M. A. Crisfield and G. Jelenić. ‘Objectivity of strain measures in the geometrically exact three-dimensional beam theory and its finite-element implementation’. In: *Proceedings of the Royal Society A-Mathematical Physical and Engineering Sciences* 455.1983 (1999), pp. 1125–1147.
DOI: 10.1098/rspa.1999.0352
- [10] R. Critchley et al. ‘A review of the manufacture, mechanical properties and potential applications of auxetic foams’. In: *physica status solidi (b)* 250.10 (2013), pp. 1963–1982.
DOI: 10.1002/pssb.201248550
- [11] I. G. Crouch. ‘Body armour – New materials, new systems’. In: *Defence Technology* 15.3 (2019), pp. 241–253.
DOI: 10.1016/j.dt.2019.02.002
- [12] *DelftBlue Supercomputer (Phase 2)*. <https://www.tudelft.nl/dhpc/ark:/44463/DelftBluePhase2>. 2024.
- [13] Dynaflow Research Group. *JIVE*. Version 3.0. 1st Apr. 2021.
URL: <https://dynaflow.com/software/jive/>
- [14] T. Gärtner et al. ‘Geometric effects on impact mitigation in architected auxetic metamaterials’. In: *Mechanics of Materials* 191 (Apr. 2024), p. 104952.
DOI: 10.1016/j.mechmat.2024.104952
- [15] T. Gärtner et al. ‘(In)efficacy of auxetic metamaterials for impact mitigation’. In: *International Journal of Impact Engineering* 206 (Dec. 2025), p. 105402.
DOI: 10.1016/j.ijimpeng.2025.105402
- [16] T. Gärtner et al. ‘A strategy for scaling the hardening behavior in finite element modelling of geometrically exact beams’. In: *Computational Mechanics* 75.5 (May 2025), pp. 1471–1482.
DOI: 10.1007/s00466-024-02572-3
- [17] L. J. Gibson et al. ‘The mechanics of two-dimensional cellular materials’. In: *Proceedings of the Royal Society of London. A. Mathematical and Physical Sciences* 382.1782 (1997), pp. 25–42.
DOI: 10.1098/rspa.1982.0087
- [18] M.-F. Guo, H. Yang and L. Ma. ‘3D lightweight double arrow-head plate-lattice auxetic structures with enhanced stiffness and energy absorption performance’. In: *Composite Structures* 290 (2022).
DOI: 10.1016/j.compstruct.2022.115484
- [19] L. Herrböck, A. Kumar and P. Steinmann. ‘Geometrically exact elastoplastic rods: determination of yield surface in terms of stress resultants’. In: *Computational Mechanics* 67.3 (2021), pp. 723–742.
DOI: 10.1007/s00466-020-01957-4

- [20] L. Herrnböck, A. Kumar and P. Steinmann. ‘Two-scale off-and online approaches to geometrically exact elastoplastic rods’. In: *Computational Mechanics* 71.1 (2022), pp. 1–24.
DOI: 10.1007/s00466-022-02204-8
- [21] L. Jiang and H. Hu. ‘Low-velocity impact response of multilayer orthogonal structural composite with auxetic effect’. In: *Composite Structures* 169 (2017), pp. 62–68.
DOI: 10.1016/j.compstruct.2016.10.018
- [22] P. Jiao et al. ‘Mechanical metamaterials and beyond’. In: *Nat Commun* 14.1 (2023), p. 6004.
DOI: 10.1038/s41467-023-41679-8
- [23] W. Liu et al. ‘In-plane dynamic crushing of re-entrant auxetic cellular structure’. In: *Materials & Design* 100 (2016), pp. 84–91.
DOI: 10.1016/j.matdes.2016.03.086
- [24] P. P. Meyer, T. Tancogne-Dejean and D. Mohr. ‘Non-symmetric plate-lattices: Recurrent neural network-based design of optimal metamaterials’. In: *Acta Materialia* 278 (2024).
DOI: 10.1016/j.actamat.2024.120246
- [25] P. P. Meyer et al. ‘Graph-based metamaterials: Deep learning of structure-property relations’. In: *Materials & Design* 223 (2022).
DOI: 10.1016/j.matdes.2022.111175
- [26] W. E. Milne. ‘Numerical Integration of Ordinary Differential Equations’. In: *The American Mathematical Monthly* 33.9 (1926).
DOI: 10.1080/00029890.1926.11986619
- [27] H. Z. Munthe-Kaas. ‘Lie Group Integrators’. In: *Encyclopedia of Applied and Computational Mathematics*. Ed. by B. Engquist. Berlin, Heidelberg: Springer Berlin Heidelberg, 2015, pp. 787–790.
DOI: 10.1007/978-3-540-70529-1_122
- [28] J. Pan et al. ‘Study on the performance of energy absorption structure of bridge piers against vehicle collision’. In: *Thin-Walled Structures* 130 (2018), pp. 85–100.
DOI: 10.1016/j.tws.2018.05.008
- [29] C. Pardini and L. Anselmo. ‘Assessing the Risk of Orbital Debris Impact’. In: *Space Debris* 1.1 (1999), pp. 59–80.
DOI: 10.1023/a:1010066300520
- [30] C. Qi et al. ‘Impact and close-in blast response of auxetic honeycomb-cored sandwich panels: Experimental tests and numerical simulations’. In: *Composite Structures* 180 (2017), pp. 161–178.
DOI: 10.1016/j.compstruct.2017.08.020
- [31] E. Reissner. ‘On Finite Deformations of Space-Curved Beams’. In: *Zeitschrift für Angewandte Mathematik Und Physik* 32.6 (1981), pp. 734–744.
DOI: 10.1007/Bf00946983
- [32] X. Ren et al. ‘Auxetic metamaterials and structures: a review’. In: *Smart Materials and Structures* 27.2 (2018).
DOI: 10.1088/1361-665X/aaa61c
- [33] D. Ruan et al. ‘In-plane dynamic crushing of honeycombs—a finite element study’. In: *International Journal of Impact Engineering* 28.2 (2003), pp. 161–182.
DOI: 10.1016/s0734-743x(02)00056-8
- [34] D. Saini and B. Shafei. ‘Prediction of extent of damage to metal roof panels under hail impact’. In: *Engineering Structures* 187 (2019), pp. 362–371.
DOI: 10.1016/j.engstruct.2019.02.036
- [35] M. Sanami et al. ‘Auxetic Materials for Sports Applications’. In: *Procedia Engineering* 72 (2014), pp. 453–458.
DOI: 10.1016/j.proeng.2014.06.079
- [36] K. K. Saxena, R. Das and E. P. Calius. ‘Three Decades of Auxetics Research – Materials with Negative Poisson’s Ratio: A Review’. In: *Advanced Engineering Materials* 18.11 (2016), pp. 1847–1870.
DOI: 10.1002/adem.201600053

- [37] J. C. Simo. ‘A finite strain beam formulation. The three-dimensional dynamic problem. Part I’. In: *Computer Methods in Applied Mechanics and Engineering* 49.1 (1985), pp. 55–70.
DOI: 10.1016/0045-7825(85)90050-7
- [38] J. C. Simo and L. Vu-Quoc. ‘A three-dimensional finite-strain rod model. part II: Computational aspects’. In: *Computer Methods in Applied Mechanics and Engineering* 58.1 (1986), pp. 79–116.
DOI: 10.1016/0045-7825(86)90079-4
- [39] C. W. Smith, J. N. Grima and K. E. Evans. ‘A novel mechanism for generating auxetic behaviour in reticulated foams: missing rib foam model’. In: *Acta Materialia* 48.17 (2000), pp. 4349–4356.
DOI: 10.1016/s1359-6454(00)00269-x
- [40] Smriti et al. ‘A thermoelastoplastic theory for special Cosserat rods’. In: *Mathematics and Mechanics of Solids* 24.3 (2018), pp. 686–700.
DOI: 10.1177/1081286517754132
- [41] J. U. Surjadi and C. M. Portela. ‘Enabling three-dimensional architected materials across length scales and timescales’. In: *Nat Mater* 24.4 (2025), pp. 493–505.
DOI: 10.1038/s41563-025-02119-8
- [42] D. Tahir, M. Zhang and H. Hu. ‘Auxetic Materials for Personal Protection: A Review’. In: *physica status solidi (b)* 259.12 (2022).
DOI: 10.1002/pssb.202200324
- [43] P. Wriggers and J. C. Simo. ‘A Note on Tangent Stiffness for Fully Nonlinear Contact Problems’. In: *Communications in Applied Numerical Methods* 1.5 (1985), pp. 199–203.
DOI: 10.1002/cnm.1630010503
- [44] J. Zhang et al. ‘Buckle-Barrel Correspondence Based on Topological Polarization Conversion in Mechanical Metamaterials’. In: *Adv Mater* 37.15 (2025), e2415962.
DOI: 10.1002/adma.202415962

A Additional number of unit cells plots

A.1 Re-entrant unit cells

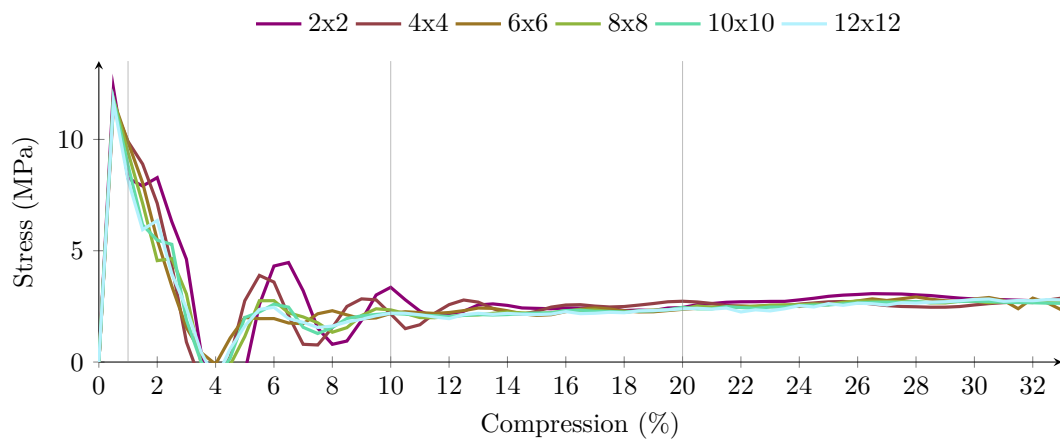


Figure A.1: Stress-strain curves of patches with a different number of re-entrant unit cells under *slow* rate compression.

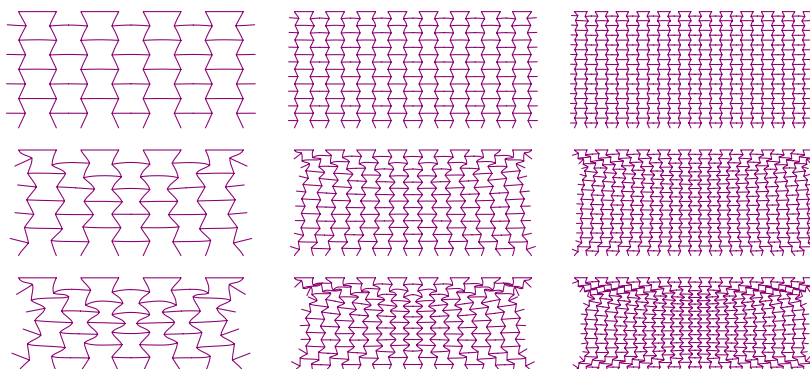


Figure A.2: Re-entrant 4×4 (left), 8×8 (centre), and 12×12 (right) unit cell patches under *slow* rate deformation at 1%, 10% and 20% compression.

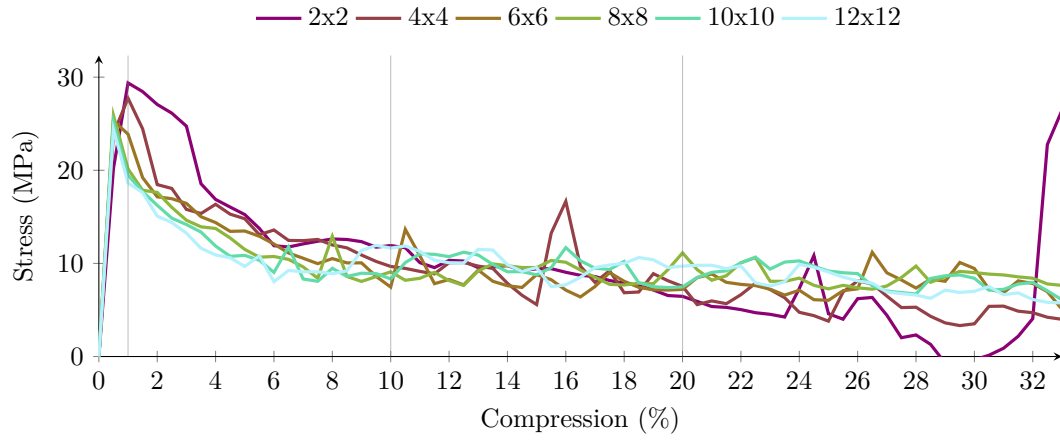


Figure A.3: Stress-strain curves of patches with a different number of re-entrant unit cells under *medium* rate compression.

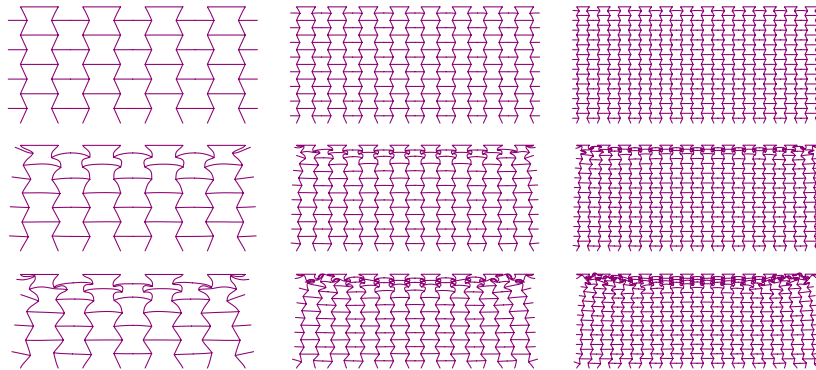


Figure A.4: Re-entrant 4×4 (left), 8×8 (centre), and 12×12 (right) unit cell patches under *medium* rate deformation at 1%, 10% and 20% compression.

A.2 Chiral unit cells

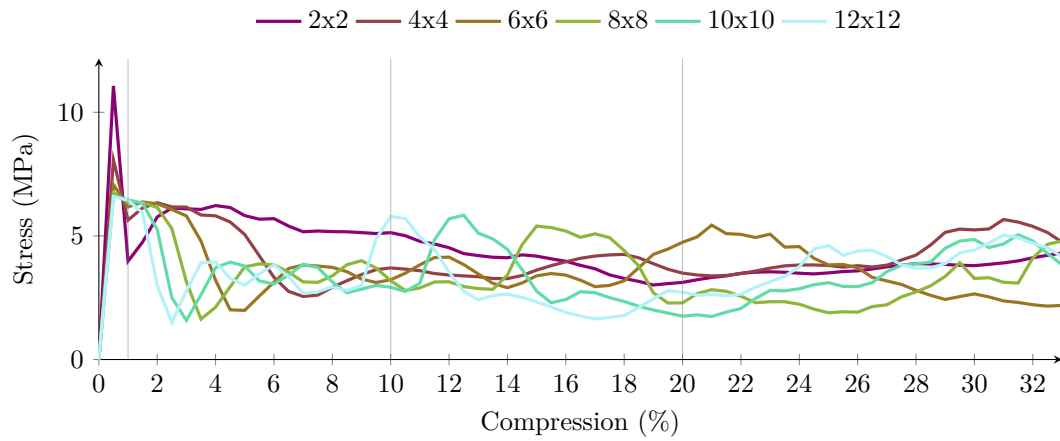


Figure A.5: Stress-strain curves of patches with a different number of chiral unit cells under *slow* rate compression.

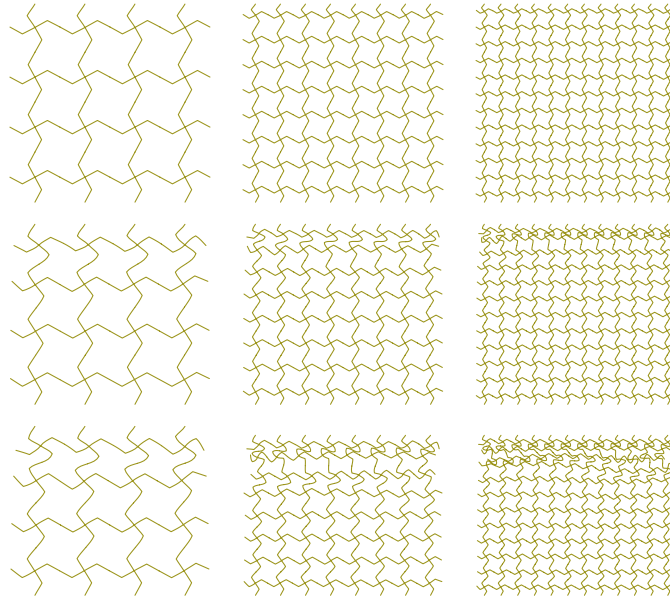


Figure A.6: Chiral 4×4 (left), 8×8 (centre), and 12×12 (right) unit cell patches under *slow* rate deformation at 1%, 10% and 20% compression.

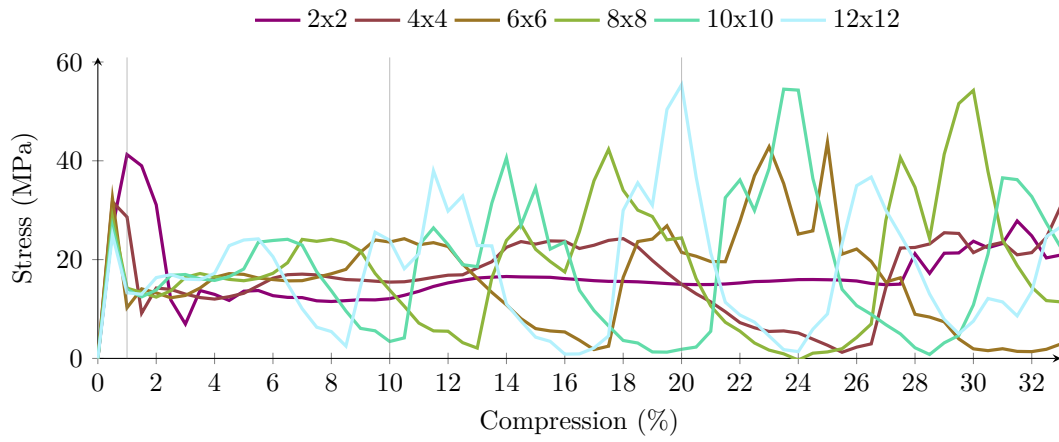


Figure A.7: Stress-strain curves of patches with a different number of chiral unit cells under *medium* rate compression.

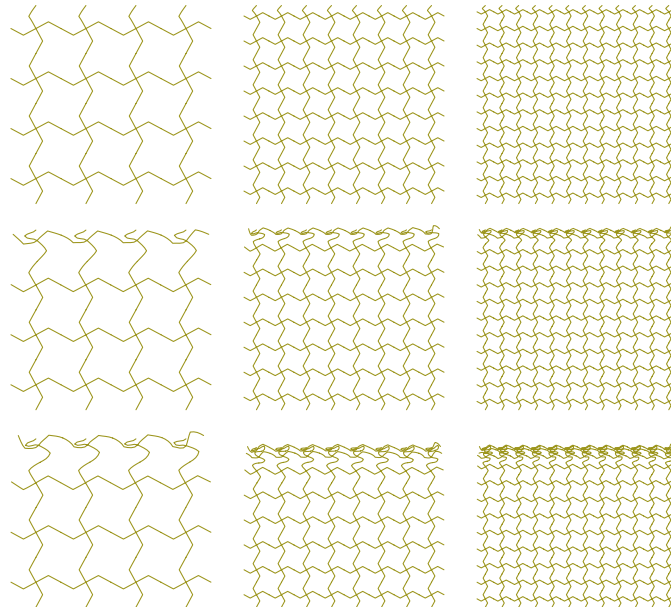


Figure A.8: Chiral 4×4 (left), 8×8 (centre), and 12×12 (right) unit cell patches under *medium* rate deformation at 1%, 10% and 20% compression.

A.3 Honeycomb unit cells

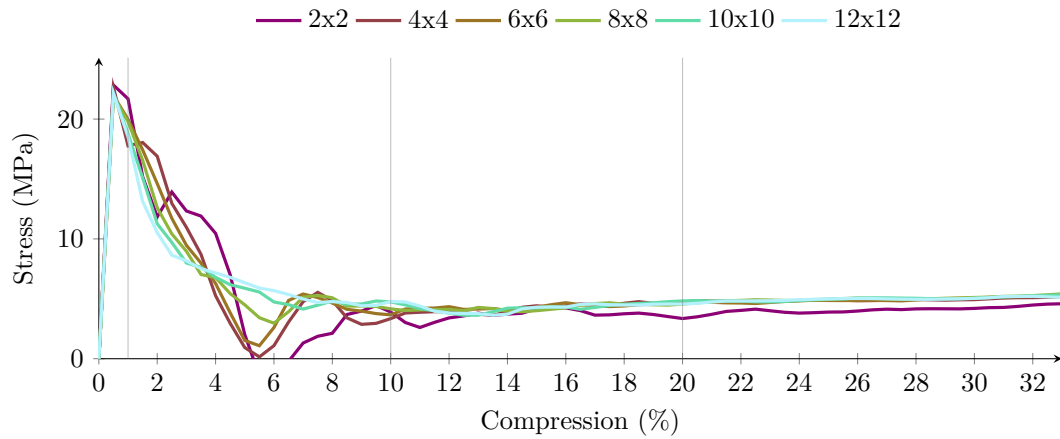


Figure A.9: Stress-strain curves of patches with a different number of honeycombs unit cells under *slow* rate compression.

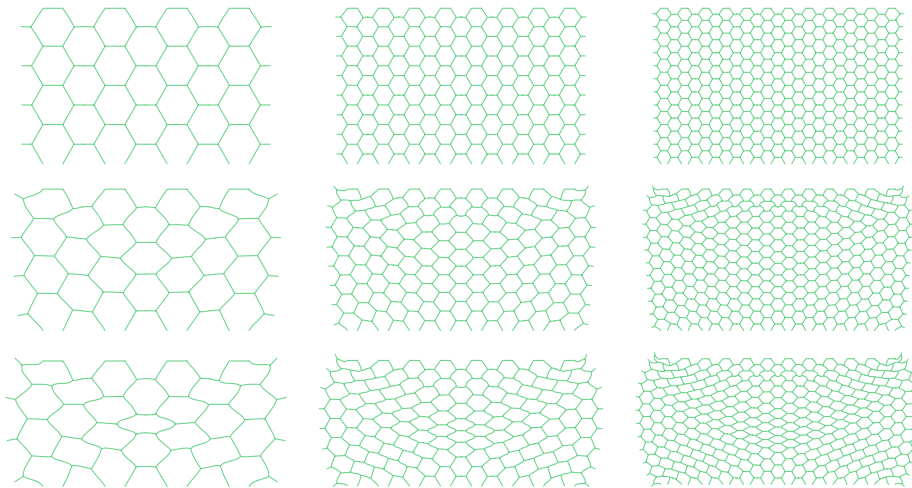


Figure A.10: 4×4 (left), 8×8 (centre), and 12×12 (right) unit cell patches under *slow* rate deformation at 1%, 10% and 20% compression.

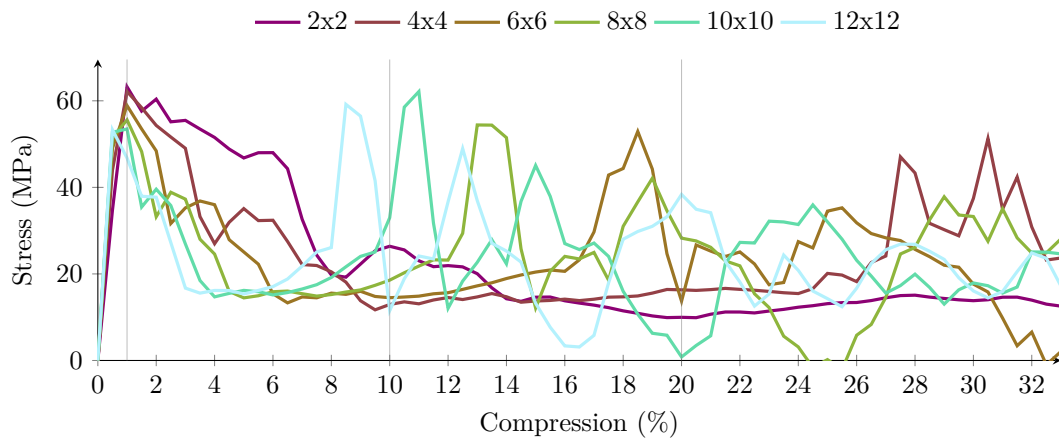


Figure A.11: Stress-strain curves of patches with a different number of honeycombs unit cells under *medium* rate compression.

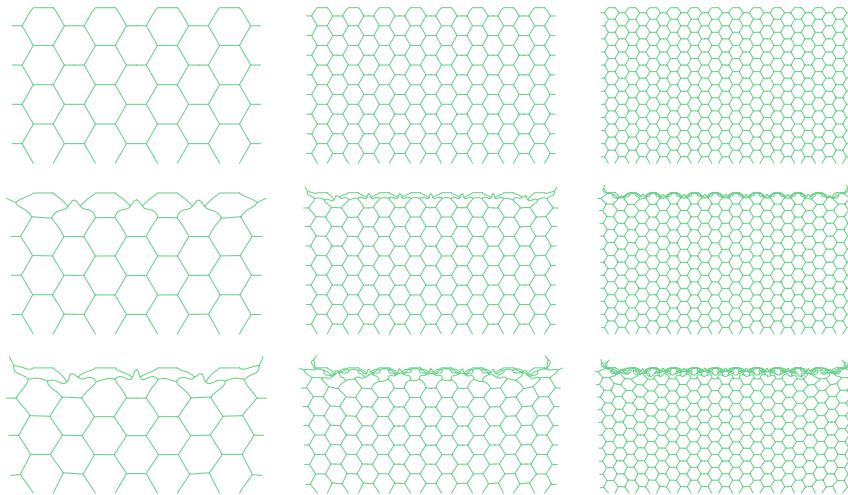


Figure A.12: 4×4 (left), 8×8 (centre), and 12×12 (right) unit cell patches under *medium* rate deformation at 1%, 10% and 20% compression.

B Additional strain rate plots

B.1 Re-entrant patch

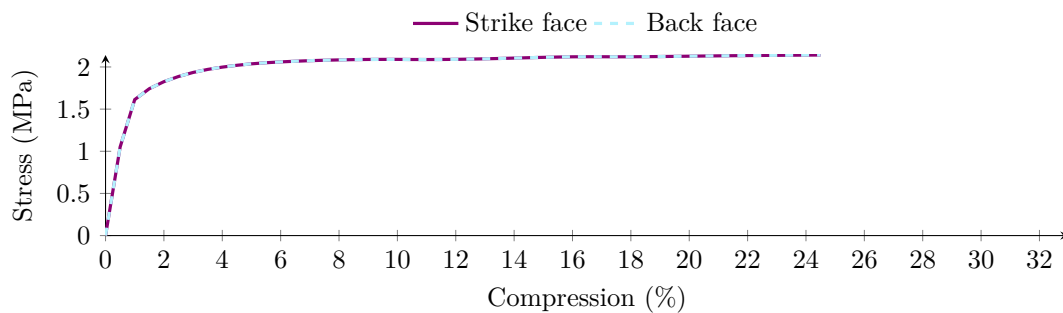


Figure B.1: Comparison of the stress on the strike face and the back face under *static* compression for an 8×8 re-entrant patch.

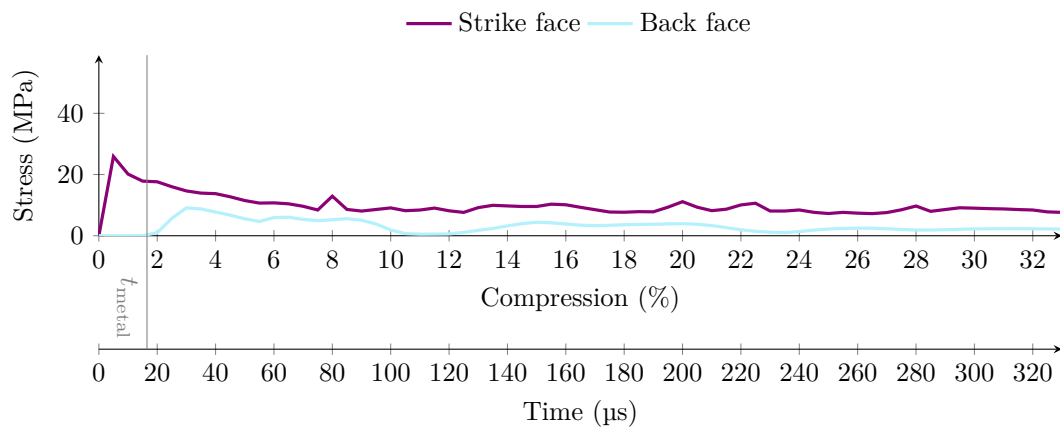


Figure B.2: Comparison of the stress on the strike face and the back face under *medium* compression for an 8×8 re-entrant patch.

B.2 Chiral patch

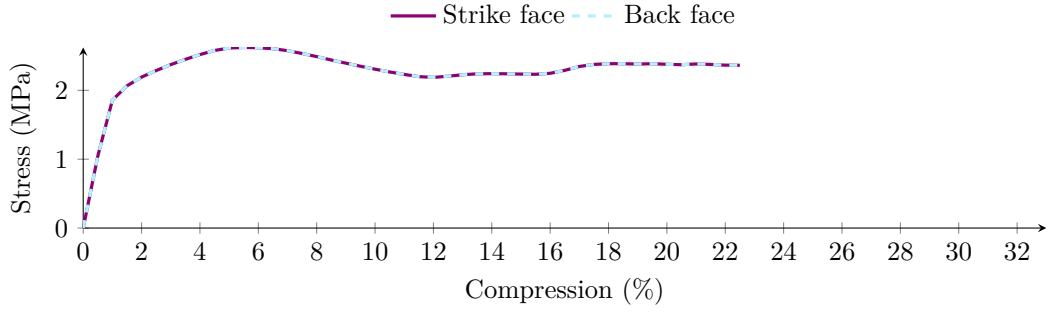


Figure B.3: Comparison of the stress on the strike face and the back face under *static* compression for an 8×8 chiral patch.

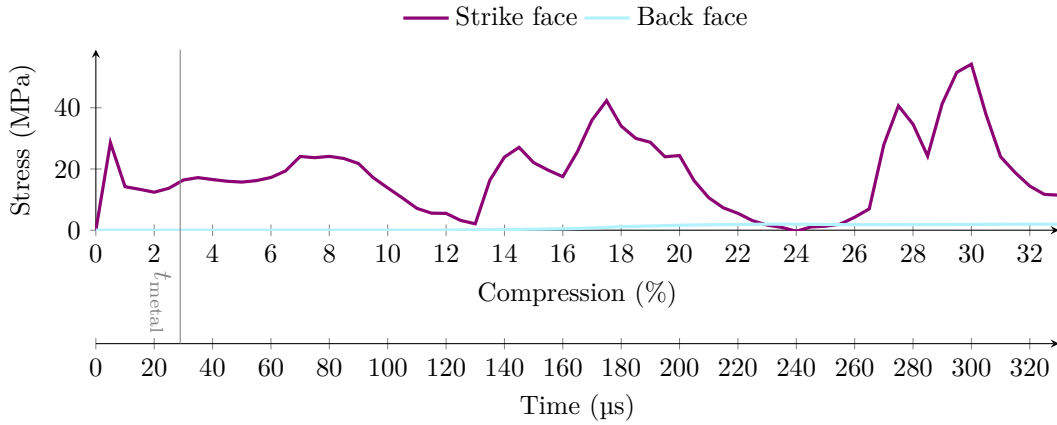


Figure B.4: Comparison of the stress on the strike face and the back face under *medium* compression for an 8×8 chiral patch.

For the chiral patch, the time needed for a pressure stress wave to travel through the metal is computed from the height of the patch $h = 132$ mm and the angle between the beams and the vertical of $\alpha = 28.1^\circ$:

$$t_{\text{metal}} = \frac{h/\cos(\alpha)}{c_{\text{metal}}} \approx 28.9 \mu\text{s}. \quad (10)$$

B.3 Honeycomb patch

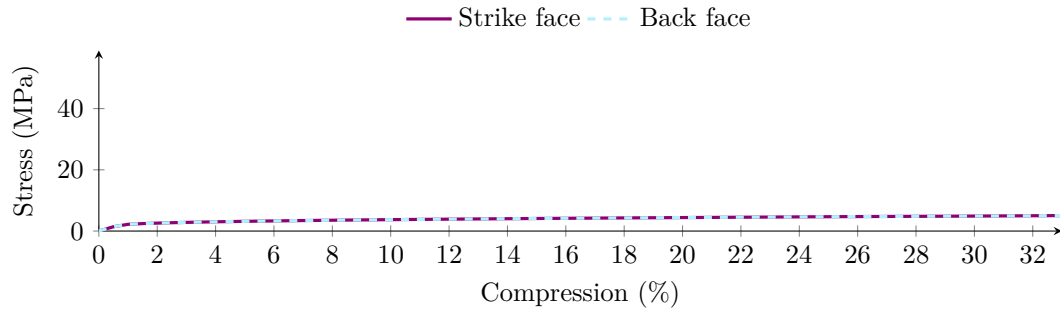


Figure B.5: Comparison of the stress on the strike face and the back face under *static* compression for an 8×8 honeycomb patch.

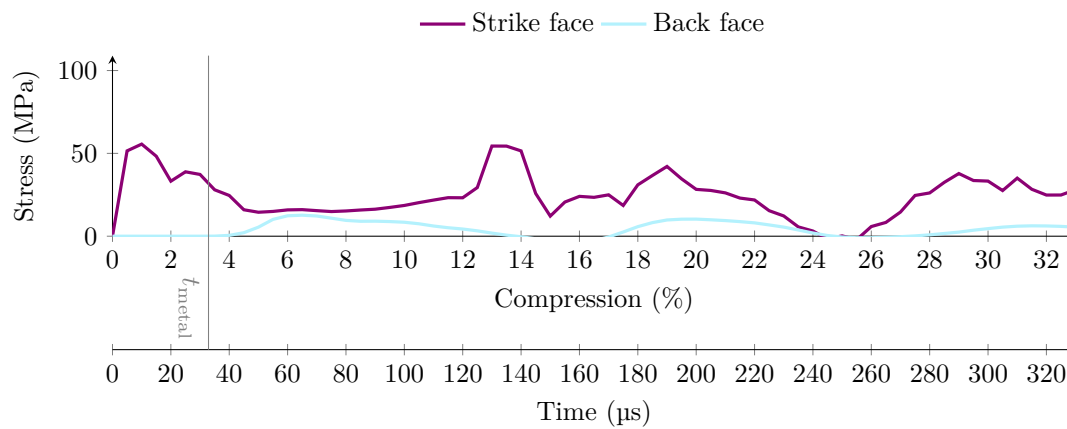


Figure B.6: Comparison of the stress on the strike face and the back face under *medium* compression for an 8×8 honeycomb patch.

For the honeycomb patch, the time needed for a pressure stress wave to travel through the metal is computed from the height of the patch $h = 148$ mm and the angle between the beams and the vertical of $\alpha = 29.7^\circ$:

$$t_{\text{metal}} = \frac{h/\cos(\alpha)}{c_{\text{metal}}} \approx 32.9 \mu\text{s}. \quad (11)$$